

Riemannian Neural Geodesic Interpolant

Jiawen Wu

*Academy of Mathematics and Systems Science, Chinese Academy of Sciences
University of Chinese Academy of Sciences*

wujiawen19@mails.ucas.ac.cn

Bingguang Chen

School of Mathematics and Statistics, Fujian Normal University

bgchen@fjnu.edu.cn

Yuyi Zhou

*Academy of Mathematics and Systems Science, Chinese Academy of Sciences
University of Chinese Academy of Sciences*

zhouyuyi23@mails.ucas.ac.cn

Qi Meng

Academy of Mathematics and Systems Science, Chinese Academy of Sciences

meq@amss.ac.cn

Rongchan Zhu

Beijing Institute of Technology

zhurongchan@126.com

Zhi-Ming Ma

Academy of Mathematics and Systems Science, Chinese Academy of Sciences

mazm@amt.ac.cn

Abstract

Stochastic interpolants are efficient generative models that bridge two arbitrary probability density functions in finite time, enabling flexible generation from the source to the target distribution or vice versa. These models are primarily developed in Euclidean space, and are therefore limited in their application to many distribution learning problems defined on Riemannian manifolds in real-world scenarios. In this work, we introduce the *Riemannian Neural Geodesic Interpolant* (RNGI) model, which interpolates between two probability densities on a Riemannian manifold along the stochastic geodesics, and then samples from one endpoint as the final state using the continuous flow originating from the other endpoint. We prove that the temporal marginal density of RNGI solves a transport equation on the Riemannian manifold. After training the model's the neural velocity and score fields, we propose the *Embedding Stochastic Differential Equation* (E-SDE) algorithm for stochastic sampling of RNGI. E-SDE significantly improves the sampling quality by reducing the accumulated error caused by the excessive intrinsic discretization of Riemannian Brownian motion in the classical *Geodesic Random Walk* (GRW) algorithm. We also provide theoretical bounds on the generative bias measured in terms of KL-divergence. Finally, we demonstrate the effectiveness of the proposed RNGI and E-SDE through experiments conducted on both collected and synthetic distributions on \mathbb{S}^2 and $\mathbf{SO}(3)$.

1 Introduction

Stochastic interpolants (Albergo & Vanden-Eijnden, 2023; Albergo et al., 2023; Chen et al., 2024) are a type of generative models that use continuous-time stochastic processes with smooth path to precisely bridge two arbitrary probability density functions in finite time. These interpolants theoretically follow a transport equation from source distribution to target distribution, and their structures leads to simpler optimization loss function compared to the normalizing flow approach in the stage of training and leverages efficient numerical schemes of stochastic differential equations in the stage of sampling. It is regarded as a unifying framework for flow-based and diffusion-based generative models and demonstrates its efficiency on practical density estimation or image generation tasks.

Stochastic interpolants are primarily developed in the Euclidean space, but in many real applications, it's more mathematically rigorous to regard the livespace of data as a curved Riemannian manifold instead of Euclidean space. For example, the data distributed on earth lives in the spherical surface (i.e., \mathbb{S}^2) in geoscience (Karpatne et al., 2019), and the molecular data satisfying 3d rotational equivariance live in $\mathbf{SO}(3)$ group in molecular biology (Jumper et al., 2021). Generative modeling for these data with geometric structure benefits from the specialized geometric model, which is established in the Riemannian rather than the Euclidean sense to approximate stochastic law latently dominated by the curvature of space more accurately. Without the prior-encoding of specific Riemannian structures, conventional Euclidean models fail to adequately capture the intrinsic spatial information embedded in data when directly applied to non-Euclidean tasks, e.g., assigning a non-zero probability to regions outside the desired manifold.

To ensure appropriate representation learning and better generation performance on Riemannian manifolds, we developed a generative model named *Riemannian Neural Geodesic Interpolant* in this work. The RNGI is a continuous-time stochastic process defined on a Riemannian manifold \mathcal{M} , connecting two probability distributions along the stochastic geodesics in the finite temporal interval $[0, 1]$, then can generate from the endpoint distribution via efficient samplers. We summarize the main technical **contributions** based on the proposed RNGI as follows.

- We extend the theoretical framework of stochastic interpolants to Riemannian manifolds, and prove that the temporal marginal probability density of RNGI solves a transport equation on Riemannian manifold under mild integrable condition of the velocity field.
- By specifying the interpolating path as geodesics, we design a quadratic loss function for learning the velocity field of the RNGI and apply implicit score matching technique for learning the score field. We further provide theoretical bounds on the generative bias measured in terms of Wasserstein-2 distance between target and the neural approximated probability distributions in Proposition 10.
- We explore efficient sampling algorithms based on the learned vector field. We apply both Geodesic Random Walk method and Embedding SDE method to numerically simulate the stochastic differential equation corresponding to the transport equation, where the Embedding SDE method is proposed to reduce the accumulated error caused by the excessive discretization of Riemannian Brownian motion in the GRW method.
- We conduct experiments on benchmark datasets which are distributed on manifolds \mathbb{S}^2 and $\mathbf{SO}(3)$. Results show the flexible interpolating ability, higher likelihood compared to the baseline generative models and the improved generation performance with E-SDE method of RNGI.

1.1 Related Work

We briefly review the related work on generative models on Riemannian manifolds. One type of work is to generalize the flow-based generative models to Riemannian manifold. The RCNF (Mathieu & Nickel, 2020) and RNODE (Lou et al., 2020) generalize the two famous Euclidean flow-based model Normalizing Flow (Rezende & Mohamed, 2015) and Neural ODE (Chen et al., 2018) to Riemannian setting. Both works build ODE flow path for sampling and train the model with log likelihood-related loss, relying on adjoint computation of projected ODE solver on \mathcal{M} . In (Rezende et al., 2020), the proposed method straightforwardly constructs normalizing flow on \mathbb{S}^2 and \mathbb{T}^2 by combining geometric operation blocks. (Rozen et al., 2021; Ben-Hamu et al., 2022) formulate the flow process via transport equations and approximate the path of transportation by divergence-based loss functions. (Chen & Lipman, 2024) generalizes the Euclidean flow matching technique to Riemannian setting by defining the conditional flow as the integral curve of vector field, then matches the field via Riemannian distance on \mathcal{M} .

The other type of work constructs the diffusion-based generative models on Riemannian manifolds. The RSGM (De Bortoli et al., 2022) model generalizes the score-based diffusion model (Song et al., 2021), deriving the forward-backward perturbing-sampling SDE and approximates the unknown heat kernel on manifold by both Sturm-Liouville decomposition and Varadhan's asymptotic. And concurrently (Huang et al., 2022) establish the Riemannian diffusion model from the perspective of variational inference by optimizing the

proposed Riemannian CT-ELBO, which is proven to be equivalent to the score-matching loss. (Jo & Hwang, 2024) generalizes diffusion bridges (Liu et al., 2023a) to manifold setting, conditioning the destination of SDE at empirical distribution of training samples then matching the bridge model from both endpoints. As another genre, (Park et al., 2022) doesn’t rely on the forward-backward scheme but directly consider parameterized Riemannian SDE, expressed in local coordinates, as universal transformer from the initial to the terminal distribution, and tunes the NN-surrogated drift and diffusion coefficient based on optimal transportation.

Different from these methods, our proposed RNGI model generalizes the stochastic interpolants to Riemannian manifolds, which can be regarded as a unifying framework for flows and diffusions.

2 Preliminaries

2.1 Stochastic Interpolant

We begin by recalling the stochastic interpolant on Euclidean space (Albergo & Vanden-Eijnden, 2023). Let $\{\Omega, \mathcal{F}, \mathbb{P}\}$ be a probability space, x_0 and x_1 be two random variables from Ω to \mathbb{R}^d . A stochastic interpolant between x_0 and x_1 is a stochastic process defined as:

$$x_t = I(t; x_0, x_1), \quad (1)$$

where $I \in C^2([0, 1]; C^2(\mathbb{R}^d \times \mathbb{R}^d))$ denotes a differentiable bridge process such that

$$I(0; x_0, x_1) = x_0, \quad I(1; x_0, x_1) = x_1.$$

The stochastic interpolant x_t is a continuous-time stochastic process whose realizations are samples from the distribution of x_0 at $t = 0$ and from the distribution of x_1 at $t = 1$ by construction. Specifically, the initial distribution x_0 can, but not necessarily, be chosen as simple uniform distribution $U(\mathbb{R}^d)$ or Gaussian distribution $N(\mathbb{R}^d)$, while x_1 , may be fairly complex, models the unknown distribution of the observational data.

2.2 Riemannian Manifold

This paper considers complete, connected, smooth Riemannian manifolds \mathcal{M} equipped with Riemannian metric g as basic domain over which the generative model is learned. The tangent space of \mathcal{M} at point x is denoted by $T_x\mathcal{M}$ and g defines an inner product over the tangent space denoted $\langle u, v \rangle_g, u, v \in T_x\mathcal{M}$. $T\mathcal{M} = \cup_{x \in \mathcal{M}} \{x\} \times T_x\mathcal{M}$ is the tangent bundle that collects all the tangent space of the manifold. The norm on Euclidean space and tangent space will be both denoted by $|\cdot|$. We use ∇ and \mathbf{div} to denote the gradient operator and divergence operator with respect to the spatial variable x on \mathcal{M} , respectively. Readers may refer to Appendix A or (Lee, 2013) for a more comprehensive background on Riemannian manifolds.

Throughout this paper, $\mathcal{X}(\mathcal{M})$ is the space of vector fields on \mathcal{M} , $C(\mathcal{M})$ is the space of continuous functions on \mathcal{M} , $C^n(\mathcal{M})$ is the space of n -th continuously differentiable functions on \mathcal{M} . $C^n([0, 1]; \mathcal{Y})$ denotes the space of n -th continuously differentiable functions from $[0, 1]$ to some function space \mathcal{Y} mentioned above.

3 Geodesic Interpolant on Riemannian manifold

We first define *Stochastic Interpolant* on Riemannian manifold by replacing Euclidean space with \mathcal{M} :

$$x_t = I(t; x_0, x_1) : [0, 1] \times \mathcal{M} \times \mathcal{M} \rightarrow \mathcal{M}.$$

For a generation task in practice, the initial distribution usually is chosen as a simple distribution on \mathcal{M} , e.g., uniform distribution $U(\mathcal{M})$ or Wrapped-Gaussian distribution $N(\mathcal{M})$ for sampling convenience. The marginal probability density $\rho(t, x)$ of the stochastic interpolant x_t can bridge the initial probability density ρ_0 and final probability density ρ_1 corresponding to x_0 and x_1 respectively. Although connecting x_0 and x_1 ,

the interpolant I is unfeasible to directly be used for sampling since the distribution of x_1 is intractable. In the next section, we will establish ways for sampling through analyzing the evolution of the intermediate probability density $\rho(t, x)$.

Firstly, we define the velocity field of a stochastic process as follows.

Definition 1 (Velocity field). *Let x_t be a stochastic process on Riemannian manifold \mathcal{M} which is differentiable with respect to the time variable t . The velocity field $v(t, x)$ of x_t is defined as:*

$$v(t, x) \triangleq \mathbb{E}(\partial_t x_t | x_t = x), \quad (2)$$

where $\partial_t x_t : \Omega \rightarrow T\mathcal{M}$ is a stochastic tangent field along the stochastic differentiable curve x_t .

Please note that in the above definition, the conditional expectation is taken by given $x_t = x$ and it can be locally calculated in a single tangent space $T_x\mathcal{M}$, which is the normal integral in the Euclidean space. With the well-defined velocity field, we now introduce a fundamental theorem of the evolution of the density $\rho(t, x)$, on which almost all of properties and algorithms of the model are based.

Theorem 2. *For Riemannian Stochastic Interpolant x_t on manifold \mathcal{M} with Riemannian metric g , we assume that its spatial-temporal probability density function $\rho(t, x)$ exists and $\rho(t, x) \in C^1([0, 1]; C^2(\mathcal{M}))$. Denote the velocity field defined above by $v(t, x)$, and if $v(t, x)$ satisfies the integrable condition*

$$\int_{\mathcal{M}} |v(t, x)| \rho(t, x) dM(x) < \infty, \quad (3)$$

then $\rho(t, x)$ solves the transport equation on \mathcal{M} as below:

$$\partial_t \rho + \mathbf{div}[\rho \cdot v(t, x)] = 0. \quad (4)$$

Readers may refer to the supplementary materials for complete proof of Theorem 2 and the detailed verification of 3. Next, we generalize the score function in Euclidean case to the score field on \mathcal{M} , which is a gradient field generated by scalar function $\rho(t, x)$.

Definition 3 (Score field). *Let x_t be a stochastic process living on Riemannian manifold \mathcal{M} , and its score field $s(t, x)$ is defined as:*

$$s(t, x) \triangleq \nabla \log \rho(t, x). \quad (5)$$

Consider the perturbation of velocity field as

$$v_F(t, x) = v(t, x) + \epsilon(t)s(t, x), \quad (6)$$

then the transport equation (4) can be transformed into the following Fokker-Planck Equation which is also solved by ρ

$$\partial_t \rho + \mathbf{div}(\rho \cdot v_F) = \epsilon(t)(\Delta_{\mathcal{M}})\rho, \quad (7)$$

where $\epsilon(t) \geq 0$ is a coefficient and $\Delta_{\mathcal{M}}$ denotes the Laplace-Beltrami operator on \mathcal{M} . Parallel with classical stochastic analysis theory, Fokker-Planck equation (7) on \mathcal{M} also corresponds to a stochastic differential equation on \mathcal{M} . More precisely, the solution $\rho(t, x)$ to 7 is concurrently the time-marginal probability density of \vec{X}_t that follows the stochastic differential equation as:

$$\begin{aligned} d\vec{X}_t &= v_F(t, \vec{X}_t)dt + \sqrt{2\epsilon(t)}dB_t^{\mathcal{M}}, \\ \vec{X}_t|_{t=0} &= x_0, \end{aligned} \quad (8)$$

where $B_t^{\mathcal{M}}$ is the Brownian motion on \mathcal{M} . And for the backward perturbation and backward Fokker-Planck equation

$$\begin{aligned} v_B(t, x) &= v(t, x) - \epsilon(t)s(t, x), \\ \partial_t \rho + \mathbf{div}(\rho \cdot v_B) &= -\epsilon(t)(\Delta_{\mathcal{M}})\rho, \end{aligned}$$

there is an associated backward SDE

$$\begin{aligned} d\overleftarrow{X}_t &= -v_B(1-t, \overleftarrow{X}_t)dt + \sqrt{2\epsilon(t)}dB_t^{\mathcal{M}}, \\ \overleftarrow{X}_t|_{t=0} &= x_1 \end{aligned} \quad (9)$$

whose solution $\overleftarrow{Y}_t = \overrightarrow{X}_{1-t}$. As there is no essential difference between equation 8 and equation 9, so we mainly discuss equation 8 as representative in following sections. And when we set $\epsilon(t) = 0$, both of equation 8 and equation 9 degenerate to an ODE

$$d\overleftrightarrow{X}_t = v_F(\overleftrightarrow{X}_t, t)dt, \quad (10)$$

which can be bi-directionally solved between $t = 0$ and $t = 1$.

The induced SDE (8, 9) and ODE (10) establish surrogate models X_t , equivalent to stochastic interpolant x_t in the sense of distribution and they can be used for simulation by leveraging SDE or ODE solvers on Riemannian manifold.

Till now the information of unknown data distribution ρ_1 is fully carried by the drift vector field v_F , which can be learned from data. We will introduce the learning and sampling algorithms in Section 4. Before that, we introduce the *Geodesic Interpolant* and its explicit form on example manifolds.

As the velocity field relies on the partial derivative of the interpolating path $I(t; x_0, x_1)$, we need to specify the form of I for constructing the learning algorithm of the velocity for computational tractable. In this section, we specify the stochastic interpolant $I(t; x_0, x_1)$ on \mathcal{M} as the geodesic, the shortest path connecting two random points on manifold.

Definition 4 (Riemannian Geodesic Interpolant). *Given a probability space $\{\Omega, \mathcal{F}, \mathbb{P}\}$ and two random variables $x_0, x_1 : \Omega \rightarrow \mathcal{M}$, the Geodesic Interpolant $I(t; x_0, x_1)$ between x_0 and x_1 is defined as*

$$I(t; x_0, x_1) = \text{Exp}_{x_0}(t \cdot \text{Log}_{x_0} x_1), \quad (11)$$

where Exp_{x_0} and Log_{x_0} denote the exponential and logarithm map at point x_0 respectively.

To construct the geodesic interpolant rigorously, we must ensure that the geodesics are 'uniquely reachable' on (almost) the entire \mathcal{M} . But generally speaking, the exponential and logarithm map are usually only defined in a small neighborhood of x_0 . As stochastic points on \mathcal{M} , x_0 and x_1 are not assumed to be closed with each other. Therefore, we must extend the locally defined exponential and logarithm map to almost the entire manifold, except for at most the cut locus of zero measure, which requires the manifold is geodesically complete (Lee, 2013).

Definition 5 (Geodesic completeness). *Let \mathcal{M} be a connected manifold equipped with Riemannian metric g . If for any geodesic γ_t on \mathcal{M} , the domain of γ can be extended from $[0, 1]$ to \mathbb{R}^+ , then \mathcal{M} is called as geodesically complete.*

The following theorem and its corollaries guarantee the well-posedness of the geodesic interpolant 4 even for 'distant' random points x_0 and x_1 on our concerned manifolds.

Proposition 6 ((Hopf & Rinow, 1931)). *If \mathcal{M} is a connected manifold equipped with Riemannian metric g , and $d_g(\cdot, \cdot)$ is the Riemannian distance on \mathcal{M} induced by g , then*

$$\mathcal{M} \text{ is geodesically complete} \Leftrightarrow (\mathcal{M}, d) \text{ is complete metric space.}$$

Corollary 7. (1) *If \mathcal{M} is a compact manifold, then \mathcal{M} is geodesically complete.* (2) *If \mathcal{M} is a compact and complete manifold, then there exists a geodesic on \mathcal{M} joining any two points p, q on \mathcal{M} .*

Now for a wide range of Riemannian manifolds, especially the compact ones like hypersphere, the geodesics are 'reachable' between the initial random variable x_0 and the target random variable x_1 on them. We still to make geodesics unique by discard a few singular points, i.e. the cut locus.

Definition 8 (Cut locus). *On a Riemannian manifold \mathcal{M} , a point q is called cut point to the point p if there are two or more minimizing geodesics joining p and q . The set of all such q , denote by $\mathcal{C}(p)$ is defined as the cut locus of p .*

Actually, $\mathcal{C}(p)$ is the collection of the points which make the exponential map Exp_p from p not injective, so the logarithm map $\text{Log}[\mathcal{C}(p)]$ cannot be defined. As for constructing geodesic interpolant, we must exclude $\{x_1(\omega) : x_1(\omega) \in \mathcal{C}[x_0(\omega)]\}$ from the target dataset, and project them back into $\mathcal{M} - \mathcal{C}(x_0)$ to keep the information contained in them as much as possible.

4 Neural Geodesic Interpolant Algorithm

To parameterize the geodesic interpolant model 11 and improve its generalization ability, we use neural networks as the approximators of latent vector fields on Riemannian manifold, which leads to a NN-based surrogate model - Riemannian Neural Geodesic Interpolant (RNGI).

4.1 Network training

The construction of sampling SDE 8 is based on the perturbation in Equation 6, which consists two unknown vector fields on \mathcal{M} to be learned. We use two neural networks to approximate velocity field $v(t, x)$ and the score field $s(t, x)$ and denote the approximate value as \hat{v} and \hat{s} respectively. For the learning of velocity field, we minimize the following quadratic loss function $\mathcal{L}_v[\hat{v}]$:

$$\int_0^1 \mathbb{E}_{x_t} \left[\frac{1}{2} |\hat{v}(x_t, t)|_g^2 - \langle \partial_t I(t; x_0, x_1), \hat{v}(x_t, t) \rangle_g \right] dt. \quad (12)$$

From the properties of quadratic function, the vector field defined in Definition 1 is the unique minimizer of \mathcal{L}_v in $\mathcal{X}(\mathcal{M})$. And for the learning of the score field, we optimize the implicit score-matching (ISM) loss $\mathcal{L}_s[\hat{s}]$:

$$\int_0^1 \mathbb{E}_{x_t} \left[\frac{1}{2} |\hat{s}(x_t, t)|_g^2 + \text{div} \hat{s}(x_t, t) \right] dt, \quad (13)$$

then the vector field defined in Definition 3 is the unique minimizer of \mathcal{L}_s in $\mathcal{X}(\mathcal{M})$, which has been proven in (Hyvärinen, 2005). Note that unlike denoising score-matching (DSM) loss in Diffusion Models, ISM allows for score approximation of general stochastic process x_t , without any structural constraint like Brownian motion or Ornstein-Uhlenbeck process.

Both the finding of the optimal neural network solution of 12 and 13 make up the neural approximation of geodesic interpolant, and the detailed training process is shown in Algorithm 1.

Algorithm 1 Training of velocity field $v(t, x)$ and score field $s(t, x)$

Input: Prior samples $\{x_0^{(n)}\}$, Data samples $\{x_1^{(n)}\}$, Interpolating path $I(t; x_0, x_1)$, Initialized velocity field network $v_{\theta_0}(t, x)$, Initialized score field network $s_{\eta_0}(t, x)$, Epoch number M , Batch size N

- 1: **for** $j = 1, \dots, M$ **do**
 - 2: Sample $\{t^{(i)}\} \sim \text{Uniform}[0, 1]$
 - 3: Draw a batch of data $\{x_0^{(i)}\}$ and $\{x_1^{(i)}\}$
 - 4: **for** $i = 1, \dots, N$ **do**
 - 5: Create coupled triples $[t^i, x_0^i, x_1^i]$
 - 6: Calculate interpolation point $x_t^i = I(t^i; x_0^i, x_1^i)$ and velocity $\partial_t I(t^i; x_0^i, x_1^i)$
 - 7: Calculate loss function $\mathcal{L}_v(v_\theta)$ and take gradient descent step on hyperparameter θ
 - 8: Calculate loss function $\mathcal{L}_s(s_\eta)$ and take gradient descent step on hyperparameter η
 - 9: **end for**
 - 10: **end for**
 - 11: **Return** Neural network v_{θ^*} and s_{η^*} with the optimal parameter θ^* and η^*
-

4.2 Samples generation

The marginal probability density of x_t is equal to that of X_t^{SDE} defined in Equation (8) at any time t , so sampling from the terminal distribution of x_1 with abstract form I can be realized by sampling from X_t^{SDE} , which further can be approximately implemented by numerically solving the neural parameterized stochastic differential equation on $[0, 1]$:

$$d\hat{X}_t = v_F^{\theta^*, \eta^*}(\hat{X}_t, t)dt + \sqrt{2\epsilon(t)}dB_t^{\mathcal{M}}, \quad \hat{X}_0 = x_0. \quad (14)$$

4.2.1 Geodesic Random Walk

In the context of Riemannian generative modeling, Geodesic Random Walk (GRW), as an intrinsic approach to solving Riemannian SDE without any dependencies on the ambient space, is a widely-used discretization scheme. GRW's step is based on the sampling on tangent bundles $T\mathcal{M}$ and projecting the sampled tangent vector to ambient space \mathcal{M} :

$$\hat{X}_{t+1} = \text{Exp}_{\hat{X}_t}(v_F^{\theta^*, \eta^*}(\hat{X}_t, t)\Delta t + \sqrt{2\epsilon\Delta t} \cdot Z_t), \quad (15)$$

where Δt is time step and Z_t is a Gaussian random variable in $T_{\hat{X}_t}\mathcal{M}$, and $\sqrt{\Delta t}$ comes from the second-order approximation of Riemannian Brownian motion $B_t^{\mathcal{M}}$.

It's provable that GRW defined as 15 will converge to the exact solution of 14 in the sense of semi-groups (Jørgensen, 1975). Based on the convergence result, intuitively, GRW implements a numerical scheme to model the stochastic dynamics governed by Riemannian SDE like its Euclidean counterpart. In the following context, when we mention ODE method for sampling, we mean that $\epsilon = 0$ in Equation (14).

4.2.2 Embedding SDE

Despite being a classical method for SDE discretization on \mathcal{M} , the GRW scheme may produce biased samples due to the intrinsic approximation of Brownian motion. When \mathcal{M} is compact, the exponential map used in GRW can only be bijective in a bounded domain $D \in T_{\hat{X}_t}\mathcal{M}$. But Z_t , as an unbounded Gaussian random variable in $T_{\hat{X}_t}\mathcal{M}$ to simulate the Brownian part in 14, still has probability to escape from D . Then the overstepping tangent vector will be Exp-mapped to a circular point on \mathcal{M} , generating unexpected image point and being iterated into wrong sample after multi-step updates.

So in brief, the insufficient expressivity of local coordinates injects systematic error into the GRW simulation of 14, preventing the stochastic generation scheme of SI models from competing with the deterministic scheme. Fortunately, stochastic analysis theory opens a broader view to deal with the simulation of SDE on manifold, establishing a new way to fix the locality issue.

From the perspective of topology, both of classical Whitney's Whitney (1936) and Nash's theorem (Nash, 1954) state that a m -dimensional Riemannian manifold can always be embedded in a Euclidean space with higher dimension $d \geq m + 1$, then extrinsically parameterized by the global frame in \mathbb{R}^d as

$$\mathcal{M} = \{p | p = (x_1, \dots, x_d) \in \mathbb{R}^d\}.$$

Based on such embedding, Proposition 9 gives another construction of Brownian motion on manifold.

Proposition 9 ((Hsu, 2002)). *If \mathcal{M} is a sub-manifold of \mathbb{R}^d , then we can construct the Brownian Motion $B_t^{\mathcal{M}}$ on \mathcal{M} by projecting the d -dimensional Euclidean Brownian Motion W_t in \mathbb{R}^d onto \mathcal{M} :*

$$dB_t^{\mathcal{M}} = P_\alpha(B_t^{\mathcal{M}}) \circ dW_t^\alpha, \quad (16)$$

where $P_\alpha(\cdot)$ denotes the α -th orthonormal projection operator from \mathbb{R}^d to the tangent space $T_{(\cdot)}\mathcal{M}$, ' $\circ dW_t^\alpha$ ' denotes the Stratonovich stochastic differential and the index α follows the Einstein summation convention.

Proposition 9 generates \mathcal{M} -Brownian motion $B_t^{\mathcal{M}}$ by solving Stratonovich SDE 16 in ambient Euclidean space \mathbb{R}^d without local Gaussian sampling, avoiding the accumulation of errors due to the incomplete expressiveness

of the local coordinate used by GRW. Having composed the embedding diffusion term $dB_t^{\mathcal{M}}$ and learned drift term $v_F^{\theta^*, \eta^*} : \mathcal{M} \rightarrow T\mathcal{M}$, we complete the Embedding SDE (E-SDE) scheme of 14 as

$$dX_t^{SDE} = v_F^{\theta^*, \eta^*}(t, X_t^{SDE})dt + \sqrt{2\epsilon(t)}P(X_t^{SDE}) \circ dW_t. \quad (17)$$

Contrast to the conventional GRW scheme for stochastic generation, our proposed E-SDE scheme not only achieves higher accuracy by globally simulating Riemannian Brownian motion $B_t^{\mathcal{M}}$ instead of locally sampling $Z_t\sqrt{\Delta t} \approx dB_t^{\mathcal{M}}$, but also enjoys faster convergence with the help of the developed numerical solvers of 17 in \mathbb{R}^d . (Cheng et al., 2022) has proven that the convergence order of GRW is $\mathcal{O}(\sqrt{\Delta t})$ as the stepsize $\Delta t \rightarrow 0$, and for the convergence order of various discretization schemes (Kloeden & Platen, 2011) of E-SDE, readers may refer to Table 1.

Table 1: The relation between the error and discretization stepsize of numerical schemes for SDE on Riemannian manifolds.

| schemes | orders |
|-------------------------------|---------------------------------|
| GRW: Geometric Euler-Maruyama | $\mathcal{O}(\sqrt{\Delta t})$ |
| E-SDE: Euler-Maruyama | $\mathcal{O}(\sqrt{\Delta t})$ |
| E-SDE: Euler-Heun | $\mathcal{O}(\sqrt{\Delta t})$ |
| E-SDE: Milstein | $\mathcal{O}(\Delta t)$ |
| E-SDE: Stochastic Runge-Kutta | $\mathcal{O}[(\Delta t)^{1.5}]$ |

We summarize the entire sampling process in Algorithm 2 below.

Algorithm 2 Sampling of new data from objective distribution x_1

Input: velocity field network v_{θ^*} , score field network s_{η^*} , number of steps N , diffusion coefficient $\epsilon(t)$, number of samples M , prior distribution $x_0 \sim \rho_0$

- 1: Calculate the perturbed drift: $v_F^{\theta^*, \eta^*} = v_{\theta^*} + \epsilon(t)s_{\eta^*}$ and time interval $\Delta t = \frac{1}{N}$
 - 2: **for** $i = 1, \dots, M$ **do**
 - 3: Draw new sample x_0^i from prior distribution ρ_0
 - 4: **for** $t = 0, \Delta t, \dots, N\Delta t = 1$ **do**
 - 5: Numerical simulate SDE: $dX_t = v_F^{\theta^*, \eta^*} dt + \sqrt{2\epsilon(t)}dB_t^{\mathcal{M}}$ with initial value x_0^i by GRW or ESDE
 - 6: **end for**
 - 7: **end for**
 - 8: **Return** New samples $\{x_1^i\}_{i=0}^M$ from data distribution ρ_1
-

4.3 Error estimation

For the parameterized surrogate generating process \hat{X}_t , there is always unavoidably some systematic error due to the suboptimal neural network approximation of $v_F(t, x)$. As both the interpolating process and generating process be modeled as SDE, we can bound the gap between the target distribution and the sampled distribution in the sense of Wasserstein-2 distance.

Proposition 10. *For two Riemannian stochastic process X_t and \hat{X}_t living on \mathcal{M} , whose time marginal probability density function are denoted by $\rho(t, x)$ and $\hat{\rho}(t, x)$ and corresponding velocity field denoted by $v(t, x)$ and $\hat{v}(t, x)$ respectively. If both of their density evolution satisfy transport equation, i.e.*

$$\begin{aligned} \partial_t \rho + \mathbf{div}[\rho \cdot v(t, x)] &= 0, \\ \partial_t \hat{\rho} + \mathbf{div}[\hat{\rho} \cdot \hat{v}(t, x)] &= 0. \end{aligned}$$

Then the KL divergence between the target distribution ρ_1 and generated distribution $\hat{\rho}_1$ can be integrated as:

$$\text{KL}(\rho_1 || \hat{\rho}_1) = \int_0^1 dt \int_{\mathcal{M}} \langle s - \hat{s}, v - \hat{v} \rangle_g \rho(t, x) dM(x). \quad (18)$$

Then from 18, the generative discrepancy can be jointly controlled by the approximation error of v and s .

Proposition 11. Consider two SDEs with same initial data x_0 and Brownian motion $B_t^{\mathcal{M}}$ on \mathcal{M} :

$$\begin{aligned} dX_t &= v_F(X_t, t)dt + \sqrt{2\epsilon(t)}dB_t^{\mathcal{M}}, \\ d\hat{X}_t &= \hat{v}_F(\hat{X}_t, t)dt + \sqrt{2\epsilon(t)}dB_t^{\mathcal{M}}. \end{aligned}$$

Let μ_t and $\hat{\mu}_t$ be the probability measures induced by X_t and \hat{X}_t respectively, assume that v and \hat{v} both are Lipschitz with constant L , we have

$$W_p(\mu_t, \hat{\mu}_t) \leq e^{Lt} \sup_{s \in [0, t]} \sup_{x \in \mathcal{M}} |v_F(x, s) - \hat{v}_F(x, s)|_g, \quad (19)$$

where W_p denotes the Wasserstein p -distance for $p \geq 1$. Let $t = 1$ in 19 then we have the final error estimation of $\hat{\mu}_1$.

Both of the proof of proposition 10 and 11 are collected in the Appendix B.

4.4 Interpolant construction

Next, we show the analytic form of the geodesic interpolant and construct E-SDE scheme on two important kinds of Riemannian manifolds: Hypersphere \mathbb{S}^n and (matrix) Lie group $\mathbf{SO}(3)$ for their broad-application in geometric data science. And the detailed completeness analysis of \mathbb{S}^n and $\mathbf{SO}(3)$ are in supplementary materials.

Hypersphere \mathbb{S}^n The hypersphere \mathbb{S}^n can be naturally embedded in the Euclidean space \mathbb{R}^{n+1} , and the exponential map $\text{Exp}_{(\cdot)}$ on \mathbb{S}^n can be written as

$$\text{Exp}_p(v) = \cos(|v|)p + \sin(|v|)\frac{v}{|v|}, \quad (20)$$

where p is a point on \mathbb{S}^n and v is a tangent vector in tangent space $T_p\mathbb{S}^n$ at p . Similarly the logarithm map $\text{Log}_{(\cdot)}$ can be written as:

$$\text{Log}_p(q) = \frac{\arccos\langle p, q \rangle}{|q - \langle p, q \rangle p|} [q - \langle p, q \rangle p], \quad (21)$$

where p and q both denote points on \mathbb{S}^n and $\langle \cdot, \cdot \rangle$ denotes the standard inner product in \mathbb{R}^{n+1} .

Thanks to geodesic completeness of \mathbb{S}^n , the locally defined exponential and logarithm map can be extended to the entire $\mathbb{S}^n - \{-p\}$ only by continuously lengthening v from $|v| = 1$ to $|v| \rightarrow \pi$, and for the sparsity of a single point $-p$ in \mathbb{S}^n , we do not need to exclude any point from the target dataset. Therefore, the interpolating process $I(t; x_0, x_1)$ on \mathbb{S}^n can be written as:

$$\begin{aligned} I(t; x_0, x_1) &= \text{Exp}_{x_0}(t \cdot \text{Log}_{x_0} x_1) \\ &= \cos(t \cdot |\text{Log}_{x_0} x_1|)x_0 \\ &\quad + \sin(t \cdot |\text{Log}_{x_0} x_1|)\frac{\text{Log}_{x_0} x_1}{|\text{Log}_{x_0} x_1|}. \end{aligned} \quad (22)$$

Now we construct E-SDE scheme on \mathbb{S}^n . For any fixed point $x = (x_1, \dots, x_{n+1})$ on $\mathbb{S}^n \subset \mathbb{R}^{n+1}$ and any separated point $\xi \in \mathbb{R}^{n+1}$, the projection operator P_x from \mathbb{R}^{n+1} to the tangent space $T_x\mathbb{S}^n$ at x is given by:

$$P_x(\xi) = \xi - \langle \xi, x \rangle x,$$

where $\langle \cdot, \cdot \rangle$ denotes the standard inner product in \mathbb{R}^{n+1} . So from above P 's expression in the form of geometric operator, we can also derive the matrix form of P as $(P(x)_{ij})$ by entries:

$$P(x)_{ij} = \delta_{ij} - x_i x_j.$$

where δ denotes Kronecker symbol. And substituting $P(x)_{ij}$ into 16 gives a SDE in \mathbb{R}^{d+1}

$$dB_t^i = \sum_{j=1}^{n+1} (\delta_{ij} - B_t^i B_t^j) \circ dW_t^j,$$

where B_t^i is the i -th component of B_t . The solution process B_t , also known as Stroock's representation (Stroock, 2000), is a Brownian motion living on the hypersphere \mathbb{S}^n .

Lie group: $\mathbf{SO}(3)$ The Lie algebra $\mathfrak{so}(3)$ of $\mathbf{SO}(3)$ is the space of skew-symmetric matrices, whose matrix element ω can also be expressed as a vector $\hat{\omega} = [\omega_1, \omega_2, \omega_3]$. The Rodrigues' rotation formula (Murray et al., 1994) bridges 3D rotation vector and 3D orthogonal matrix, which gives the exponential map from $\mathfrak{so}(3)$ to $\mathbf{SO}(3)$:

$$\text{Exp}_e(\omega) = I + \sin \theta \cdot \omega + (1 - \cos \theta) \cdot \omega^2, \quad (23)$$

where $\theta = \sqrt{\omega_1^2 + \omega_2^2 + \omega_3^2}$ denotes the Frobenius norm of ω , e denotes the identity element in the group. Inversely, the logarithm map from $\mathbf{SO}(3)$ to $\mathfrak{so}(3)$ at e is given by:

$$\text{Log}_e \begin{bmatrix} R_{11} & R_{12} & R_{13} \\ R_{21} & R_{22} & R_{23} \\ R_{31} & R_{32} & R_{33} \end{bmatrix} = \frac{\gamma}{2 \sin \gamma} \begin{bmatrix} R_{32} - R_{23} \\ R_{13} - R_{31} \\ R_{21} - R_{12} \end{bmatrix}, \quad (24)$$

where the rotation matrix $R \in \mathbf{SO}(3)$ is expressed by entries and rotation angle γ is calculated by

$$\gamma = \arccos\left(\frac{\text{tr}(R) - 1}{2}\right).$$

For any point $p \in \mathbf{SO}(3)$, the Exp and Log map at p are translated from those at e :

$$\begin{aligned} \text{Exp}_p(v) &= p \cdot \text{Exp}_e(p^{-1}v), \\ \text{Log}_p(q) &= p \cdot \text{Log}_e(p^{-1}q), \end{aligned}$$

where $v \in T_p \mathbf{SO}(3)$ and $q \in \mathbf{SO}(3)$. For the random variable x_0 and x_1 , the geodesic interpolant $I(t; x_0, x_1)$ on $\mathbf{SO}(3)$ is expressed as

$$\begin{aligned} I(t; x_0, x_1) &= \text{Exp}_{x_0}(t \cdot \text{Log}_{x_0} x_1) \\ &= x_0 \cdot \text{Exp}_e[t \cdot \text{Log}_e(x_0^{-1} x_1)]. \end{aligned} \quad (25)$$

The compactness of $\mathbf{SO}(3)$ makes it geodesically complete, and to ensure the uniqueness, note that the orthogonality of $\mathbf{SO}(3)$'s matrix elements has a constraint on their trace that $\text{tr}(R) \in [-1, 3]$, so choose the main value of \arccos then we get a mapped $\gamma \in [0, \pi]$. But for those matrices with $\text{tr} = -1$, which represents a rotation with angle $= \pi$, the bijection between rotation vectors and orthogonal matrices does not hold anymore, leading to **nan** value of 27. So for those datapoints $(x_0^{-1} x_1)(\omega)$ satisfying $\text{tr}[(x_0^{-1} x_1)(\omega)] = -1$, we must truncate their trace when directly construct geodesic interpolant on $\mathbf{SO}(3)$.

To construct E-SDE scheme on $\mathbf{SO}(3)$, as the embedding of $\mathbf{SO}(3)$ into \mathbb{R}^d is not as trivial as that of \mathbb{S}^n , we introduce the 'truncation-orthogonalization' embedding of $\mathbf{SO}(3)$ into \mathbb{R}^6 proposed by (Zhou et al., 2019).

For a 3-d orthogonal matrix $R = (\mathbf{r}_1, \mathbf{r}_2, \mathbf{r}_3)$, the truncating map $\mathcal{P} : \mathbf{SO}(3) \rightarrow \mathbb{R}^6$ is defined by

$$\mathcal{P}(R) = \begin{pmatrix} \mathbf{r}_1 \\ \mathbf{r}_2 \end{pmatrix}.$$

And for a vector $\mathbf{l} = \begin{pmatrix} \mathbf{l}_1 \\ \mathbf{l}_2 \end{pmatrix} \in \mathbb{R}^6$, the Gram-Schmit orgonalization of the two 3-d vectors \mathbf{l}_1 and \mathbf{l}_2 gives two orthogonal 3-d unit vectors \mathbf{r}_1 and \mathbf{r}_2 . Additionally, the cross product gives another unit vector $\mathbf{r}_3 = \mathbf{r}_1 \times \mathbf{r}_2$, which is orthogonal to both \mathbf{r}_1 and \mathbf{r}_2 . Then the orthogonalizing map $\mathcal{Q}: \mathbb{R}^6 \rightarrow \mathbf{SO}(3)$ is defined by

$$\mathcal{Q}(\mathbf{l}) = (\mathbf{r}_1, \mathbf{r}_2, \mathbf{r}_3).$$

\mathcal{P} and \mathcal{Q} establish a bijection between $\mathbf{SO}(3)$ and a submanifold \mathcal{M} of \mathbb{R}^6 . Such bijection cannot be implemented by the Euler angle embedding, axis-angle embedding or quaternion embedding. Specifically, \mathcal{M} can be further embedded as a submanifold of \mathbb{S}^5 in \mathbb{R}^6 , so the probability distribution on $\mathbf{SO}(3)$ can be transformed to be supported on $\mathcal{M} \subset \mathbb{S}^5$, which enables us to construct RNGI model and its E-SDE scheme in \mathbb{R}^6 .

5 Experiment

We apply the RNGI model to datasets living on two Riemannian manifolds: \mathbb{S}^2 and $\mathbf{SO}(3)$ to validate its effectiveness. Both of the geographical and synthetic density generation experiment aim to demonstrate the improved accuracy of RNGI models in terms of log-likelihood and E-SDE in terms of distance metric, and the distribution connection experiment aims to demonstrate the flexibility of RNGI models to generate samples of target distribution from arbitrary initial distributions. All of experiments run on a single Nvidia Geforce RTX 4090/3090 GPU.

5.1 Geographical data on earth

Many geographical and climatic events, such as volcanic eruptions (NOAA, 2020b), earthquakes (NOAA, 2020a), floods (Brakenridge, 2017), and wild fires (EOSDIS, 2020), whose occurrence can be represented as geographical coordinates on the surface of the earth, can be naturally modeled as samples drawn from latent probability distributions ρ_{event} on \mathbb{S}^2 . We use the RNGI model to bridge the uniform distribution $U(\mathbb{S}^2)$ and the unknown ρ_{event} . Then we transform new samples from $U(\mathbb{S}^2)$ into high-quality samples from ρ_{event} by the generative schemes of RNGI model.



Figure 1: Generative visualization on flood dataset. From left to right there are the ground truth data, samples from ODE, GRW and E-SDE. The diffusion coefficient of GRW and E-SDE is set to $\epsilon = 0.01$ and the sampling steps are $N = 100$.

We use two fully-connected neural network to respectively predict the velocity field and score field of the geodesic interpolant on \mathbb{S}^2 , and both of the inputs and outputs are extrinsic 3-d vector representation of spherical points. We employ 'RiemannianAdam' optimizer in package `geoopt` (Becigneul & Ganea, 2019) on volcano, earthquake and flood and AdamW on fire datasets after tuning, and train each experiment for 60000 iterations on the first three experiments and 120000 iterations on the last one. The detailed parameter settings are listed in Table 7 in the appendix C.1. The stochastic sampling via E-SDE is conducted by Euler-Heun solver of 0.5 order or Heun solver of 1.5 order in package `torchsde` (Kidger et al., 2021). And the deterministic sampling via ODE is conducted by Euler or dopri5 solver in package `torchdiffeq` (Chen,

2018). The generation results are measured by negative log-likelihood (NLL) in Table 2, which are computed from solving the likelihood ODE, parallel with the sampling ODE, by the adjoint method implemented by `torchdiffeq`, and the generative visualization is shown in Figure 1.

Table 2: Negative log-likelihood (\downarrow) results on four earth datasets. The best result is marked in bold. All numbers are averaged over 5 runs of experiments and each run contains 10 rounds of sampling. Each time of sampling generates samples of the same size as that of the primary datasets. The diffusion coefficient is fixed at $\epsilon = 0.01$ and the likelihood step is adaptive for Dopri5 solver.

| Dataset Size | Volcano 827 | Earthquake 6120 | Flood 4875 | Fire 12810 |
|-------------------------------------|-------------------------------------|------------------------------------|-----------------------------------|------------------------------------|
| RCNF (Mathieu & Nickel, 2020) | -6.05 ± 0.61 | 0.14 ± 0.23 | 1.11 ± 0.19 | -0.80 ± 0.54 |
| Moser Flow (Rozen et al., 2021) | -4.21 ± 0.17 | -0.16 ± 0.06 | 0.57 ± 0.10 | -1.28 ± 0.05 |
| CNFM (Ben-Hamu et al., 2022) | -2.38 ± 0.17 | -0.38 ± 0.01 | 0.25 ± 0.02 | -1.40 ± 0.02 |
| RFM (Chen & Lipman, 2024) | -7.93 ± 1.67 | -0.28 ± 0.08 | 0.42 ± 0.05 | -1.86 ± 0.11 |
| M-FFF (Sorrenson et al., 2024) | -2.25 ± 0.02 | -0.23 ± 0.01 | 0.51 ± 0.01 | -1.19 ± 0.03 |
| StereoSGM (De Bortoli et al., 2022) | -3.80 ± 0.27 | -0.19 ± 0.05 | 0.59 ± 0.07 | -1.28 ± 0.12 |
| RSGM (De Bortoli et al., 2022) | -4.92 ± 0.25 | -0.19 ± 0.07 | 0.45 ± 0.17 | -1.33 ± 0.06 |
| RDM (Huang et al., 2022) | -6.61 ± 0.97 | -0.40 ± 0.05 | 0.43 ± 0.07 | -1.38 ± 0.05 |
| RSGM-improved (Lou et al., 2023) | -4.69 ± 0.29 | -0.27 ± 0.05 | 0.44 ± 0.03 | -1.51 ± 0.13 |
| LogBM (Jo & Hwang, 2024) | -9.52 ± 0.87 | -0.30 ± 0.06 | 0.42 ± 0.08 | -2.47 ± 0.11 |
| RNGI(Ours) | -13.03 ± 0.64 | -0.79 ± 0.08 | 0.10 ± 0.07 | -2.31 ± 0.05 |

Under different settings of diffusion intensity coefficient ϵ , the proposed E-SDE algorithm keeps more fine-grained features compared to ODE sampler and outperforms conventional spherical GRW scheme in stochastic generative quality without sacrificing on computing efficiency. As shown in Table 3, the larger choice of ϵ perturbs the sampling results from the GRW scheme more seriously than those from the E-SDE scheme, which illustrates the improvement of sampling quality by the global construction of the diffusion part of E-SDE.

The weakness of local simulation used in GRW scheme can also be obvious when there are more discretization steps. Table 4 shows the results of the ablation study of N , where the sampling precision of E-SDE scheme benefits from the finer stepsize, but the performance of GRW scheme conversely decreases, which suffers from the inaccurate Gaussian stochastic step magnified by too much exponential projections.

Table 3: Wasserstein-2 distance (\downarrow) between the ground truth distribution and the generated distribution. The sampling steps are fixed at $N = 100$.

| Sampler | ϵ | Dataset | | | |
|---------|------------|---------|------------|--------|--------|
| | | Volcano | Earthquake | Flood | Fire |
| ODE | 0 | 0.3154 | 0.2088 | 0.2141 | 0.1729 |
| GRW | 0.1 | 0.8180 | 0.7432 | 0.7588 | 1.0596 |
| | 0.01 | 0.5467 | 0.5006 | 0.5321 | 0.6466 |
| | 0.001 | 0.3674 | 0.2952 | 0.3178 | 0.3546 |
| E-SDE | 0.1 | 0.4299 | 0.3460 | 0.3122 | 0.6883 |
| | 0.01 | 0.3326 | 0.2084 | 0.2095 | 0.2920 |
| | 0.001 | 0.3112 | 0.2035 | 0.2147 | 0.1583 |

Table 4: Wasserstein-2 distance (\downarrow) between the ground truth distribution and the generated distribution. Generated samples have the same size as that of the primary datasets. The diffusion coefficient of GRW and E-SDE is fixed at $\epsilon = 0.01$.

| Sampler | Steps | Dataset | | | |
|---------|-------|---------|------------|--------|--------|
| | | Volcano | Earthquake | Flood | Fire |
| ODE | 10 | 0.3680 | 0.2578 | 0.2572 | 0.2637 |
| | 100 | 0.3154 | 0.2088 | 0.2141 | 0.1729 |
| | 1000 | 0.3074 | 0.1975 | 0.2118 | 0.1742 |
| GRW | 10 | 0.3923 | 0.3055 | 0.3291 | 0.4569 |
| | 100 | 0.5467 | 0.5006 | 0.5321 | 0.6466 |
| | 1000 | 0.8375 | 0.7486 | 0.7679 | 0.9543 |
| E-SDE | 10 | 0.4493 | 0.2528 | 0.2453 | 0.3389 |
| | 100 | 0.3326 | 0.2084 | 0.2095 | 0.2920 |
| | 1000 | 0.2938 | 0.2114 | 0.2044 | 0.2947 |

5.2 Density generation on $\mathbf{SO}(3)$

In this experiment, we bridge the uniform distribution and various synthetic probability distributions $\mu_i (i = 1, \dots, 7)$ on $\mathbf{SO}(3)$. There are four target densities named as peak, cube, cone, line, which are designed from the symmetry of exact geometry objects in \mathbb{R}^3 , and three multi-modal target densities $\mathbb{W}^{16}, \mathbb{W}^{32}, \mathbb{W}^{64}$ which distribute as 'Wrapped Gaussian' on $\mathbf{SO}(3)$.

We train three RNGI models with different representation methods of the velocity and score field. As the element on $\mathbf{SO}(3)$ is represented by a 3×3 matrix, the RNGI-D model learns the maps between the 3×3 matrices, and then project the output matrix onto $\mathbf{SO}(3)$. The RNGI-EM and RNGI-ES models rely on the 'truncation-orthogonalization' embedding (Zhou et al., 2019) of target distributions μ_i into \mathbb{R}^6 as $\bar{\mu}_i = \mu_i \circ \mathcal{P}^{-1}$. The difference between RNGI-EM model and RNGI-ES model is that the initial distribution of RNGI-EM is embedded as $\bar{U}[\mathbf{SO}(3)] = U[\mathbf{SO}(3)] \circ \mathcal{P}^{-1}$ and that of RNGI-ES is directly $U(\mathbb{S}^5)$.

Table 5: Log-likelihood (\uparrow) results(1) in density generation experiments on $\mathbf{SO}(3)$. The log-likelihood of initial samples are converted to 0 uniformly. All numbers are averaged over 5 runs of experiments and each run contains 10 rounds of sampling. Each time of sampling generates samples of the same size as that of the primary datasets. All of ODEs are numerically solved by dopri5 solver.

| Dataset Size | peak 600000 | cube 600000 | cone 600000 | line 600000 |
|---|----------------|----------------|----------------|----------------|
| RCNF(Mathieu & Nickel, 2020) | 13.47 | 1.02 | 8.82 | -0.0026 |
| RELIE(Falorsi et al., 2019) | 0.00 | 3.27 | 5.32 | -6.97 |
| IPDF(Murphy et al., 2021) | 7.30 | 4.33 | 4.75 | 1.12 |
| Mixture-MF(Mohlin et al., 2020) | 10.52 | 4.52 | 8.36 | 0.77 |
| Moser Flow(Rozen et al., 2021) | 11.15 | 4.42 | 8.22 | 1.38 |
| $\mathbf{SO}(3)$ -NF(Mobius)(Liu et al., 2023b) | 13.93 | 4.81 | 8.98 | 1.38 |
| $\mathbf{SO}(3)$ -NF(Affine)(Liu et al., 2023b) | 13.50 | 0.00 | 8.84 | 0.00 |
| RNGI-D | 14.52 | 1.84 | 6.05 | 0.00 |
| RNGI-EM | 20.46 | 5.06 | 12.08 | 2.87 |
| RNGI-ES | 26.27 | 14.16 | 19.76 | 10.15 |

While training RNGI-D model, we parameterize the velocity and score field with two fully-connected neural networks $v^\theta(t, x)$ and $s^\eta(t, x)$ whose depth is 6 and width is 512. The spatial input of v^θ are the 9-d flatten

Table 6: Log-likelihood (\uparrow) results(2) in density generation experiments on $\mathbf{SO}(3)$. The log-likelihood of initial samples are converted to 0 uniformly. All numbers are averaged over 5 runs of experiments and each run contains 10 rounds of sampling, and \pm represents the standard deviation of the interval with a 95% confidence level. Each time of sampling generates samples of the same size as that of the primary datasets. All of ODEs are numerically solved by dopri5 solver.

| Dataset Size | \mathbb{W}^{16} 600000 | \mathbb{W}^{32} 600000 | \mathbb{W}^{64} 600000 |
|---|------------------------------------|------------------------------------|------------------------------------|
| Moser Flow(Rozen et al., 2021) | 5.21 ± 0.03 | 4.53 ± 0.03 | 3.87 ± 0.02 |
| $\mathbf{SO}(3)$ -NF(Liu et al., 2023b) | 5.17 ± 0.01 | 4.48 ± 0.004 | 3.75 ± 0.01 |
| M-FFF(Sorrenson et al., 2024) | 5.23 ± 0.02 | 4.57 ± 0.02 | 3.91 ± 0.02 |
| StereoSGM(De Bortoli et al., 2022) | 5.23 ± 0.04 | 4.52 ± 0.03 | 3.78 ± 0.04 |
| RSGM(De Bortoli et al., 2022) | 5.25 ± 0.03 | 4.56 ± 0.03 | 3.87 ± 0.02 |
| RNGI-D | 3.04 ± 0.03 | 2.56 ± 0.02 | 2.01 ± 0.03 |
| RNGI-EM | 7.76 ± 0.04 | 5.43 ± 0.03 | 3.98 ± 0.01 |
| RNGI-ES | 14.94 ± 0.05 | 13.89 ± 0.04 | 12.64 ± 0.05 |

vector of the 3×3 matrix for stronger expressivity, and that for s^η are 3-d axis-angle vector of 3-d rotation matrix for more efficient divergence computation. Both of the dimensionality of the output of $v^\theta(t, x)$ and $s^\eta(t, x)$ are as same as the input. Then we optimize the networks with linear-scheduled AdamW and train 50000 iterations. In the sampling stage, we directly apply Dopri5 solver in `torchdiffeq` package to solve matrix-valued ODE 10, and implement the geometric Euler-Maruyama solver for matrix-valued SDE in `pytorch`.

For RNGI-EM and RNGI-ES models, the parameterization of velocity and score field is established on \mathbb{S}^5 . Therefore the two neural vector field, similarly parameterized by MLPs of size 6×512 , take 6-d representation both as their input and output, whose expressivity and computational efficiency come from the flat geometry of \mathbb{R}^6 . The optimizers and samplers are the same as RNGI-D, besides that the solver for E-SDE is Heun’s. Both of the detailed parameter settings used for RNGI-D, RNGI-EM and RNGI-ES models are listed in Table 8 in the appendix C.1.

The generative visualization are shown in the appendix C.3, where the visualization follows (Murphy et al., 2021; Liu et al., 2023b). Particularly, when sampling via ODE scheme, we use the adjoint method in (Mathieu & Nickel, 2020) to evaluate the log-likelihood as quality measure. The results are reported in shown in Table 5 and Table 6 with baselines taken from (Liu et al., 2023b) and (Sorrenson et al., 2024), which shows that both of RNGI-EM and RNGI-ES models reach higher log-likelihood than baseline methods, and RNGI-ES model reports the best performance.

The RNGI-EM/ES models can not only generate new samples with higher accuracy, but also produce less computational cost in both training and sampling stage. One single training iteration of RNGI-D model takes 2.5s - 3s on a NVIDIA RTX 3090 GPU but that of RNGI-EM/ES model only takes 0.025s - 0.4s, because the flatten representation used by the velocity network and the axis-angle representation used by the score network of RNGI-D model make the loss surface stiff and the gradient computation harder, therefore slow down the back propagation. In the sampling stage, to generate $600000 \times 20\% = 120000$ new samples, RNGI-E model takes 9.5s and 4.3s using E-SDE and ODE schemes respectively, and the time cost for the GRW and ODE schemes of RNGI-D model are 12.6s and 5.6s. Note that RNGI-E and RNGI-D models take 6-d vector and 3×3 matrix as their data format separately, thus the former consumes a third less memory usage compared to the latter.

5.3 Interpolation between mixture densities

Another advantage of RNGI models is that it does not restrict the sampling process to start from the uniform distribution or any projected distribution from a single tangent space like wrapped Gaussian distribution

(Mardia & Jupp, 2009) as traditional diffusion models. To demonstrate the flexibility on the initial distribution, we also use the RNGI models to interpolate between the two multi-modal densities with different modals on \mathbb{S}^2 and $\mathbf{SO}(3)$. Intuitively, the models are trained to push different density centers to merge or pull them to split, which is a challenging task due to the non-flat geometry of \mathbb{S}^2 and $\mathbf{SO}(3)$.

On \mathbb{S}^2 , we train RNGI model to connect two K -center VMF mixture distributions \mathbb{V}^K (Mardia & Jupp, 2009). The setting of two endpoint distributions are $\mathbb{V}^{32} \leftrightarrow \mathbb{V}^8$, $\mathbb{V}^{64} \leftrightarrow \mathbb{V}^8$, $\mathbb{V}^{64} \leftrightarrow \mathbb{V}^{16}$ and $\mathbb{V}_{\{\mu_i\}}^{32} \rightarrow \mathbb{V}_{\{\nu_i\}}^{32}$ respectively, where \leftrightarrow means the generation is conducted for both directions. The K centers of \mathbb{V}^K are random points on \mathbb{S}^2 that are drawn from $U(\mathbb{S}^2)$ and all of the concentration parameters κ are uniformly set to 256. As for $\mathbf{SO}(3)$, we train RNGI-D and RNGI-E model for the interpolation between wrapped K -mixture Gaussian distributions \mathbb{W}^K . The setting of K for \mathbb{W}^K is the same as that of \mathbb{V}^K , and the position of centers and scaling parameters are $p_i \sim U[\mathbf{SO}(3)]$ and $\sigma_i^2 = 0.01$.

We use MLPs of size 6×1024 , who are also optimized by linear-scheduled AdamW with 50000 iterations, to parameterize the two vector fields in both \mathbb{S}^2 and $\mathbf{SO}(3)$ experiments. All of the parameter settings of network training are same and shown in Table 8 in Appendix C.1. And we calculate the K – L divergence between ground truth distribution and generated distribution as the metric of precision.

The bi-directional numerical results and generative visualization are collected in Appendix C.2 and C.3. As shown in them, both of RNGI model on \mathbb{S}^2 and RNGI-D/E models on $\mathbf{SO}(3)$ can connect and convert two complex densities on their living manifolds. On \mathbb{S}^2 , the E-SDE scheme generates the most realistic two endpoint VMF mixture densities, where ODE scheme distorts the centers into ‘ribbons’ and GRW scheme generates many points out of distributions. And on $\mathbf{SO}(3)$, while the training of RNGI-D model is similarly much slower than RNGI-E model, both models capture the main feature of the two multi-modal endpoint densities. The generative style of the two models are slightly different that RNGI-D are more serrated and RNGI-E are more diffusive, and RNGI-E model and its E-SDE scheme suffer from much less computational burden as their training is not as computationally-intensive as RNGI-D model and its GRW scheme.

6 Conclusion

In this work, we propose *Riemannian Neural Geodesic Interpolant*, a generative model capable of bridging two arbitrary probability distributions on Riemannian manifolds. Based on the RNGI, we design learning and sampling algorithms for density generation on Riemannian manifold \mathbb{S}^2 and $\mathbf{SO}(3)$. Our model shows significant flexibility in bridging complex distributions and exhibits observable improvement in sampling quality with the E-SDE sampler. Furthermore, the RNGI model still has the potential to be practically deployed in broader generation tasks defined on various Riemannian manifolds. For instance, we will extend the RNGI from point generation to point cloud generation on general submanifolds in \mathbb{R}^d in the future.

Acknowledgments

We express thanks to Xiangdong Li, Fuzhou Gong and Xicheng Zhang for the mathematical discussions, and Hongsheng Qi for his support on the computational resources.

References

- Takuya Akiba, Shotaro Sano, Toshihiko Yanase, Takeru Ohta, and Masanori Koyama. Optuna: A next-generation hyperparameter optimization framework. In *Proceedings of the 25th ACM SIGKDD international conference on knowledge discovery & data mining*, pp. 2623–2631, 2019.
- Michael S. Albergo, Nicholas M. Boffi, and Eric Vanden-Eijnden. Stochastic interpolants: A unifying framework for flows and diffusions. *arXiv*, 2023. URL <https://arxiv.org/abs/2303.08797>.
- Michael Samuel Albergo and Eric Vanden-Eijnden. Building normalizing flows with stochastic interpolants. In *The Eleventh International Conference on Learning Representations*, ICLR, 2023. URL <https://openreview.net/forum?id=li7qeBbCR1t>.
- Gary Becigneul and Octavian-Eugen Ganea. Riemannian adaptive optimization methods. In *International Conference on Learning Representations*, ICLR, 2019. URL <https://openreview.net/forum?id=r1eiqi09K7>.
- Heli Ben-Hamu, Samuel Cohen, Joey Bose, Brandon Amos, Maximilian Nickel, Aditya Grover, Ricky T. Q. Chen, and Yaron Lipman. Matching normalizing flows and probability paths on manifolds. In *International Conference on Machine Learning*, ICML, 2022. URL <https://api.semanticscholar.org/CorpusID:250340682>.
- G.R. Brakenridge. Global active archive of large flood events. <http://floodobservatory.colorado.edu/Archives/>, 2017.
- Ricky T. Q. Chen. torchdiffeq. <https://github.com/rtqichen/torchdiffeq>, 2018.
- Ricky T. Q. Chen and Yaron Lipman. Flow matching on general geometries. In *The Twelfth International Conference on Learning Representations*, ICLR, 2024. URL <https://openreview.net/forum?id=g7ohD1TITL>.
- Ricky T. Q. Chen, Yulia Rubanova, Jesse Bettencourt, and David K Duvenaud. Neural ordinary differential equations. In S. Bengio, H. Wallach, H. Larochelle, K. Grauman, N. Cesa-Bianchi, and R. Garnett (eds.), *Advances in Neural Information Processing Systems*, NeurIPS, 2018. URL https://proceedings.neurips.cc/paper_files/paper/2018/file/69386f6bb1dfed68692a24c8686939b9-Paper.pdf.
- Yifan Chen, Mark Goldstein, Mengjian Hua, Michael S. Albergo, Nicholas M. Boffi, and Eric Vanden-Eijnden. Probabilistic forecasting with stochastic interpolants and föllmer processes. In *Proceedings of the 41st International Conference on Machine Learning*, ICML, 2024.
- Xiang Cheng, Jingzhao Zhang, and Suvrit Sra. Efficient sampling on riemannian manifolds via langevin MCMC. In Alice H. Oh, Alekh Agarwal, Danielle Belgrave, and Kyunghyun Cho (eds.), *Advances in Neural Information Processing Systems*, 2022.
- Valentin De Bortoli, Emile Mathieu, Michael Hutchinson, James Thornton, Yee Whye Teh, and Arnaud Doucet. Riemannian score-based generative modelling. In *Advances in Neural Information Processing Systems*, NeurIPS, 2022.
- EOSDIS. Active fire data. <https://earthdata.nasa.gov/earth-observation-data/near-real-time/firms/active-fire-data>, 2020.
- Luca Falorsi, Pim de Haan, Tim R. Davidson, and Patrick Forré. Reparameterizing distributions on lie groups. In Kamalika Chaudhuri and Masashi Sugiyama (eds.), *Proceedings of the Twenty-Second International Conference on Artificial Intelligence and Statistics*, volume 89 of *AISTATS*, pp. 3244–3253. PMLR, 16–18 Apr 2019. URL <https://proceedings.mlr.press/v89/falorsi19a.html>.
- H. Hopf and W. Rinow. Ueber den begriff der vollständigen differentialgeometrischen fläche. *Commentarii mathematici Helvetici*, 3:209–225, 1931. URL <http://eudml.org/doc/138562>.
- Elton P Hsu. *Stochastic analysis on manifolds*. Number 38. American Mathematical Soc., 2002.

-
- Chin-Wei Huang, Milad Aghajohari, Avishek Joey Bose, Prakash Panangaden, and Aaron Courville. Riemannian diffusion models. In *Proceedings of the 36th International Conference on Neural Information Processing Systems*, NeurIPS, 2022. ISBN 9781713871088.
- Aapo Hyvärinen. Estimation of non-normalized statistical models by score matching. *Journal of Machine Learning Research*, 6(24):695–709, 2005. URL <http://jmlr.org/papers/v6/hyvarinen05a.html>.
- Jaehyeong Jo and Sung Ju Hwang. Generative modeling on manifolds through mixture of riemannian diffusion processes. In *Forty-first International Conference on Machine Learning*, ICML, 2024. URL <https://openreview.net/forum?id=60HydCpCMZ>.
- Erik Jørgensen. The central limit problem for geodesic random walks. *Zeitschrift für Wahrscheinlichkeitstheorie und Verwandte Gebiete*, 32:1–64, 1975. URL <https://api.semanticscholar.org/CorpusID:120031766>.
- John Jumper, Richard Evans, Alexander Pritzel, Tim Green, Michael Figurnov, Olaf Ronneberger, Kathryn Tunyasuvunakool, Russ Bates, Augustin Židek, Anna Potapenko, et al. Highly accurate protein structure prediction with alphafold. *nature*, 596(7873):583–589, 2021.
- Anuj Karpatne, Imme Ebert-Uphoff, Sai Ravela, Hassan Ali Babaie, and Vipin Kumar. Machine learning for the geosciences: Challenges and opportunities. In *IEEE Transactions on Knowledge and Data Engineering*, TKDE, 2019. doi: 10.1109/TKDE.2018.2861006.
- Patrick Kidger, James Foster, Xuechen Li, Harald Oberhauser, and Terry Lyons. Neural SDEs as Infinite-Dimensional GANs. In *International Conference on Machine Learning*, ICML, 2021.
- P.E. Kloeden and E. Platen. *Numerical Solution of Stochastic Differential Equations*. Stochastic Modelling and Applied Probability. Springer Berlin Heidelberg, 2011. ISBN 9783540540625.
- John M. Lee. *Introduction to Smooth Manifolds*. Graduate Texts in Mathematics. Springer New York, NY, 2013.
- Xingchao Liu, Lemeng Wu, Mao Ye, and qiang liu. Learning diffusion bridges on constrained domains. In *The Eleventh International Conference on Learning Representations*, ICLR, 2023a. URL <https://openreview.net/forum?id=WH1yCa0TbB>.
- Yulin Liu, Haoran Liu, Yingda Yin, Yang Wang, Baoquan Chen, and He Wang. Delving into discrete normalizing flows on $so(3)$ manifold for probabilistic rotation modeling. In *2023 IEEE/CVF Conference on Computer Vision and Pattern Recognition*, CVPR, 2023b. doi: 10.1109/CVPR52729.2023.02037.
- Aaron Lou, Derek Lim, Isay Katsman, Leo Huang, Qingxuan Jiang, Ser Nam Lim, and Christopher M De Sa. Neural manifold ordinary differential equations. In *Advances in Neural Information Processing Systems*, NeurIPS, 2020. URL https://proceedings.neurips.cc/paper_files/paper/2020/file/cbf8710b43df3f2c1553e649403426df-Paper.pdf.
- Aaron Lou, Minkai Xu, Adam Farris, and Stefano Ermon. Scaling riemannian diffusion models. In *Proceedings of the 37th International Conference on Neural Information Processing Systems*, NeurIPS, 2023.
- K.V. Mardia and P.E. Jupp. *Directional Statistics*. Wiley Series in Probability and Statistics. Wiley, 2009. ISBN 9780470317815. URL <https://books.google.com/books?id=PTNiCm4Q-MOC>.
- Emile Mathieu and Maximilian Nickel. Riemannian continuous normalizing flows. In *Proceedings of the 34th International Conference on Neural Information Processing Systems*, NeurIPS, 2020. ISBN 9781713829546.
- David Mohlin, Josephine Sullivan, and Gérald Bianchi. Probabilistic orientation estimation with matrix fisher distributions. In *Advances in Neural Information Processing Systems*, NeurIPS, 2020. URL https://proceedings.neurips.cc/paper_files/paper/2020/file/33cc2b872dfe481abef0f61af181dfcf-Paper.pdf.

-
- Kieran A Murphy, Carlos Esteves, Varun Jampani, Srikumar Ramalingam, and Ameesh Makadia. Implicit-pdf: Non-parametric representation of probability distributions on the rotation manifold. In *Proceedings of the 38th International Conference on Machine Learning, ICML, 2021*. URL <https://proceedings.mlr.press/v139/murphy21a.html>.
- Richard M. Murray, Zexiang Li, and Shankar Sastry. *A Mathematical Introduction to Robotic Manipulation*. CRC Press, 1994.
- John Nash. C1 isometric imbeddings. *Annals of Mathematics*, 60(3):383–396, 1954. ISSN 0003486X, 19398980. URL <http://www.jstor.org/stable/1969840>.
- NOAA. Ncei/wds global significant earthquake database. <https://www.ncei.noaa.gov/access/metadata/landing-page/bin/iso?id=gov.noaa.ngdc.mgg.hazards:G012153>, 2020a.
- NOAA. Ncei/wds global significant volcanic eruptions database. <https://www.ncei.noaa.gov/access/metadata/landing-page/bin/iso?id=gov.noaa.ngdc.mgg.hazards:G10147>, 2020b.
- Sung Woo Park, Hyomin Kim, Kyungjae Lee, and Junseok Kwon. Riemannian neural SDE: Learning stochastic representations on manifolds. In *Advances in Neural Information Processing Systems*, NeurIPS, 2022. URL <https://openreview.net/forum?id=1ryTomA0iKa>.
- Danilo Rezende and Shakir Mohamed. Variational inference with normalizing flows. In *Proceedings of the 32nd International Conference on Machine Learning, ICML, 2015*. URL <https://proceedings.mlr.press/v37/rezende15.html>.
- Danilo Jimenez Rezende, George Papamakarios, Sébastien Racanière, Michael S. Albergo, Gurtej Kanwar, Phiala E. Shanahan, and Kyle Cranmer. Normalizing flows on tori and spheres. In *Proceedings of the 37th International Conference on Machine Learning, ICML, 2020*.
- Noam Rozen, Aditya Grover, Maximilian Nickel, and Yaron Lipman. Moser flow: Divergence-based generative modeling on manifolds. In *Neural Information Processing Systems*, NeurIPS, 2021. URL <https://api.semanticscholar.org/CorpusID:237194783>.
- Yang Song, Jascha Sohl-Dickstein, Diederik P Kingma, Abhishek Kumar, Stefano Ermon, and Ben Poole. Score-based generative modeling through stochastic differential equations. In *International Conference on Learning Representations, ICLR, 2021*. URL <https://openreview.net/forum?id=PXTIG12RRHS>.
- Peter Sorrenson, Felix Draxler, Armand Rousselot, Sander Hummerich, and Ullrich Koethe. Learning distributions on manifolds with free-form flows. In *The Thirty-eighth Annual Conference on Neural Information Processing Systems*, NeurIPS, 2024. URL <https://openreview.net/forum?id=QbPHYPKJJI>.
- D.W. Stroock. *An Introduction to the Analysis of Paths on a Riemannian Manifold*. Mathematical surveys and monographs. American Mathematical Society, 2000. ISBN 9780821838396. URL <https://books.google.com/books?id=loS992htI3kC>.
- Hassler Whitney. Differentiable manifolds. *Annals of Mathematics*, 37(3):645–680, 1936. ISSN 0003486X, 19398980.
- Yi Zhou, Connelly Barnes, Jingwan Lu, Jimei Yang, and Hao Li. On the continuity of rotation representations in neural networks. In *Proceedings of the IEEE/CVF conference on computer vision and pattern recognition*, pp. 5745–5753, 2019.

A Stochastic Differential Geometry

In this section, we list some fundamental concepts and notations in stochastic differential geometry.

We begin with some preliminaries of smooth manifold. And see Lee (2013) for a more detailed and comprehensive account. A smooth d -dimensional manifold is a topological space \mathcal{M} and a family of pairs (called charts) $\{(U_i, \varphi_i)\}$, where the $\{U_i\}$ are open cover of \mathcal{M} and φ_i is a homeomorphism from U_i to an open subset of \mathbb{R}^d . The charts are required to satisfy a compatibility condition: if $U_i \cap U_j = U$, then $\varphi_i \circ \varphi_j^{-1}|_U$ is a smooth map from $\varphi_j(U)$ to $\varphi_i(U)$. The set of smooth functions on \mathcal{M} is denoted $C^\infty(\mathcal{M})$ whose element has type $f : \mathcal{M} \rightarrow \mathbb{R}$ such that for any chart (U, φ) the map $f \circ \varphi^{-1}$ is smooth.

Definition 12. For a given point $x \in \mathcal{M}$, a derivation at x is a linear operator $D : C^\infty(\mathcal{M}) \rightarrow \mathbb{R}$ such that for all $f, g \in C^\infty(\mathcal{M})$,

$$D(fg) = f(x)D(g) + g(x)D(f).$$

The derivation at x is also called the tangent vector at x . The set of all tangent vectors is a d -dimensional real vector space called the tangent space $T_x\mathcal{M}$. The tangent bundle is denoted by $T\mathcal{M}$, consists of the tangent space $T_x\mathcal{M}$ at all points x in \mathcal{M} :

$$T\mathcal{M} = \bigsqcup_{x \in \mathcal{M}} T_x\mathcal{M} = \{(x, v_x) | x \in \mathcal{M}, v_x \in T_x\mathcal{M}\}.$$

Every smooth manifold can be embedded in \mathbb{R}^m with $m > d$ for some suitably chosen m . We can view $T_x\mathcal{M}$ as a linear subspace of $T_x\mathbb{R}^m$, thus a tangent vector can be written as:

$$D = \sum_{j=1}^d d_j \frac{\partial}{\partial x_j}.$$

A vector field X is a continuous map such that for each point x on the manifold, $X(x) \in T_x\mathcal{M}$. Such a vector field can also map any smooth function f to a function, via the assignment $x \in \mathcal{M} \rightarrow X(x)(f) \in \mathbb{R}$. If $X(\cdot)(f)$ is smooth we say that the vector field is smooth. The space of smooth vector fields on \mathcal{M} is denoted by $\mathcal{X}(\mathcal{M})$.

Every smooth manifold \mathcal{M} can be equipped with a Riemannian metric g . g is a metric tensor field such that for each $x \in \mathcal{M}$, g defines an inner product $g(x) : T_x\mathcal{M} \times T_x\mathcal{M} \rightarrow \mathbb{R}$ on the tangent space. For any $X, Y \in \mathcal{X}(\mathcal{M})$, we denote $\langle X, Y \rangle_g = g(X, Y)$ with $g(X, Y)(x) = g_x(X(x), Y(x))$. Note that in local coordinates we can define $G = \{g_{ij}\} = \{g(X_i, X_j)\}$ where $\{X_i\}_{1 \leq i \leq d}$ is a basis of the tangent space. This allows us to write the metric using the coordinates

$$\langle X, Y \rangle_g = \sum_{i,j} x_i y_j g_{ij}.$$

The Riemannian metric allows us to define a measure over measurable subsets of the manifold. For a single chart (U, φ) and any smooth function f supported in U , consider the following positive linear functional:

$$f \mapsto \int_{\varphi(U)} (f \sqrt{|\det G|}) \circ \varphi^{-1} dx = \int_U f dM_U,$$

where M_U is a unique Borel measure given by Riesz representation theorem. Then a partition of unity method allows us to extend M_U to be defined over the entire \mathcal{M} , which leads to the Riemannian measure M . A probability density function p over \mathcal{M} can be thought of as a non-negative function satisfying $\int_{\mathcal{M}} p dM = 1$.

A crucial structure closely related to the Riemannian metric is the gradient operator on \mathcal{M} . For any $f \in C^\infty(\mathcal{M})$ and $Y \in \mathcal{X}(\mathcal{M})$, the gradient operator ∇ is defined via $\langle \nabla f, Y \rangle_g = Y(f)$. The divergence operator \mathbf{div} (or $\nabla \cdot$) can be obtained via the following Stokes formula: for any $f \in C^\infty(\mathcal{M})$ and any $X \in \mathcal{X}(\mathcal{M})$, $\int_{\mathcal{M}} \mathbf{div} X f dM = - \int_{\mathcal{M}} X(f) dM$. The Laplace-Beltrami operator $\Delta_{\mathcal{M}}$ is given by $\Delta_{\mathcal{M}} f := \mathbf{div}(\nabla f)$.

We now turn to stochastic differential equations on \mathcal{M} . Solutions of stochastic differential equations on manifolds should be sought in the space of manifold-valued semimartingales. A continuous \mathcal{M} -valued stochastic process X_t is called a \mathcal{M} -valued semimartingale if for any $f \in C^\infty(\mathcal{M})$ we have that $f(X_t)$ is a real valued semimartingale.

A stochastic differential equation on \mathcal{M} is defined by l vector fields $V_1, \dots, V_l \in \mathcal{X}(\mathcal{M})$, an \mathcal{R}^l -valued semimartingale Z , and an \mathcal{M} -valued random variable X_0 , serving as the initial value of the solution. For more details we refer to Hsu (2002).

Definition 13. A \mathcal{M} -valued semimartingale X_t is said to be the solution of $SDE(V, Z; X_0)$ up to a stopping time τ if for any $f \in C^\infty(\mathcal{M})$ and $t \in [0, \tau]$,

$$f(X_t) = f(X_0) + \int_0^t \sum_{i=1}^l V_i(f)(X_s) \circ dZ_s^i.$$

Using the Laplace–Beltrami operator, we can give the definition of the Brownian motion on \mathcal{M} as a diffusion process.

Definition 14. Let $B_t^\mathcal{M}$ be a \mathcal{M} -valued semimartingale. We say $B_t^\mathcal{M}$ is a Brownian motion on \mathcal{M} if for any $f \in C^\infty(\mathcal{M})$, the following process is a real local martingale:

$$f(B_t^\mathcal{M}) - f(B_0^\mathcal{M}) - \frac{1}{2} \int_0^t \Delta_\mathcal{M} f(B_s^\mathcal{M}) ds.$$

This definition considers Brownian motion as a diffusion process generated by the Laplace–Beltrami operator $\frac{\Delta_\mathcal{M}}{2}$, and is shown to be equivalent to several other descriptions, including the one stating that it is a semimartingale whose anti-development with the Levi-Civita connection is a Euclidean Brownian motion. Meanwhile, it is much more convenient to use equivalent characterizations such as embedding Euclidean brownian motion or Stroock’s representation when considering realization.

B Theoretical guarantee of RNGI

Proof of Theorem 2 For a wide range of test function $\varphi(x)$ on \mathcal{M} , we have

$$\begin{aligned} \mathbb{E}\varphi(x_t) &= \int_{\mathcal{M}} \varphi(x) \rho(t, x) dM(x), \\ \frac{d}{dt} \mathbb{E}\varphi(x_t) &= \int_{\mathcal{M}} \varphi(x) \partial_t \rho(t, x) dM(x). \end{aligned}$$

At the same time, the time derivative of expectation can also be calculated as

$$\begin{aligned} \frac{d}{dt} \mathbb{E}\varphi(x_t) &= \mathbb{E}\left[\frac{d}{dt} \varphi(x_t)\right] = \mathbb{E}[\nabla \varphi \cdot \partial_t x_t] \\ &= \int_{\mathcal{M}} \nabla \varphi \cdot \mathbb{E}[\partial_t x_t | x_t = x] \rho(t, x) dM(x) \\ &= \int_{\mathcal{M}} \nabla \varphi \cdot v(t, x) \rho(t, x) dM(x) \\ &= \int_{\mathcal{M}} -\varphi \cdot \mathbf{div} v(t, x) \rho(t, x) dM(x). \end{aligned}$$

Combine above two equation we have

$$\int_{\mathcal{M}} \varphi \cdot \{\partial_t \rho(t, x) + \mathbf{div}[v(t, x) \rho(t, x)]\} dM(x) = 0.$$

Having proved Theorem 2, we only need to verify the integrable condition on manifold we are concerned with to ensure our implement on them is theoretically solid.

Hypersphere \mathbb{S}^n We first state that Geodesic Interpolant is well-defined on almost the whole \mathbb{S}^n . Note that for $p \in \mathbb{S}^n$ and $v \in T_p \mathbb{S}^n$, when $|v| = \pi$, the corresponding point on \mathbb{S}^n is $-p$ but the injective property does not hold anymore as the non-uniqueness of the shortest path between p and $-p$. Therefore, only by considering the 'almost complete' alternative $\mathbb{S}^n - \{-p\}$, we can construct RNGI model.

Now back to our context of integrable condition. For the anti-projection, denoted as $\text{Log}_{x_0} x_1$, of the final random variable x_1 , which is a tangent vector living in $T_{x_0} \mathbb{S}^n$, We have given the expression of Geodesic Interpolant on \mathbb{S}^n as

$$\begin{aligned} I(t; x_0, x_1) &= \text{Exp}_{x_0}(t \cdot \text{Log}_{x_0} x_1) \\ &= \cos(t \cdot |\text{Log}_{x_0} x_1|) x_0 + \sin(t \cdot |\text{Log}_{x_0} x_1|) \frac{\text{Log}_{x_0} x_1}{|\text{Log}_{x_0} x_1|}. \end{aligned}$$

Then we can calculate the velocity field of the interpolating curve as:

$$\partial_t I(t; x_0, x_1) = \cos(t \cdot |\text{Log}_{x_0} x_1|) \text{Log}_{x_0} x_1 - |\text{Log}_{x_0} x_1| \sin(t \cdot |\text{Log}_{x_0} x_1|) x_0.$$

Notice that x_0 and $\text{Log}_{x_0} x_1$ are orthogonal vectors in \mathbb{R}^{n+1} , so

$$|\partial_t I(t; x_0, x_1)| = |\text{Log}_{x_0} x_1| < 2\pi,$$

where ' $<$ ' comes from the compactness of \mathbb{S}^n . And from the conditional expectation definition of $v(t, x)$ and full expectation formula we have

$$\int_{\mathcal{M}} |v(t, x)| \rho(t, x) dM(x) \leq \mathbb{E}(|\partial_t I(t; x_0, x_1)|).$$

Combine above two inequalities we finally reach the integrable condition on \mathbb{S}^n :

$$\mathbb{E}(|\partial_t I(t; x_0, x_1)|) < \infty.$$

(Matrix) Lie group For theoretical completeness, we first introduce some basic knowledge about general Lie group.

On a general Lie group G and its Lie algebra \mathfrak{g} , which can be seen as its tangent space at the identity element e , the exponential map Exp is defined by the concept of single-parameter subgroup.

For any X in Lie algebra \mathfrak{g} , let $\exp_X(t) : \mathbb{R} \rightarrow G$ denotes the unique single-parameter subgroup whose derivative at $t = 0$ is X (the existence and uniqueness of such subgroup can be found in any textbook of Lie group theory), the exponential map is defined as

$$\text{Exp}(X) = \exp_X(1),$$

and the logarithm map Log is locally defined as the inverse map of Exp without direct definition. And for those concerning Lie groups take matrices as their elements, the exponential and logarithm map have more explicit form

$$\begin{aligned} \text{Exp}(X) &= \sum_{k=0}^{\infty} \frac{1}{k!} X^k, \\ \text{Log}(R) &= \sum_{k=1}^{\infty} \frac{(-1)^{k+1}}{k} (R - I)^k, \end{aligned}$$

which are formally given by the exponential and power series of matrices and consistent with their name. Note that the symbol Exp and Log without the lower index always refer to the Exp/Log map at e , and then, carried by $\mathfrak{g} = T_e G$, be translated to any point p by the group action induced by p .

Particularly, the Rodrigues' rotation formula gives the connection between 3-D rotation vector and 3-D orthogonal matrix, which can be used to construct the bijective map between $\mathbf{SO}(3)$ and $\mathfrak{so}(3)$:

$$\text{Exp}_e(\omega) = I + \sin \theta \cdot \omega + (1 - \cos \theta) \cdot \omega^2, \quad (26)$$

where $\theta = \sqrt{\omega_1^2 + \omega_2^2 + \omega_3^2}$ denotes the norm of ω (Frobenius for ω and Euclidean for $\hat{\omega}$). And inversely, the logarithm map from $\mathbf{SO}(3)$ to $\mathfrak{so}(3)$ at e is given by:

$$\text{Log}_e \begin{bmatrix} R_{11} & R_{12} & R_{13} \\ R_{21} & R_{22} & R_{23} \\ R_{31} & R_{32} & R_{33} \end{bmatrix} = \frac{\gamma}{2 \sin \gamma} \begin{bmatrix} R_{32} - R_{23} \\ R_{13} - R_{31} \\ R_{21} - R_{12} \end{bmatrix}, \quad (27)$$

where the rotation matrix $R \in \mathbf{SO}(3)$ is expressed by entries and rotation angle γ is calculated by

$$\gamma = \arccos\left(\frac{\text{tr}(R) - 1}{2}\right).$$

Similarly to \mathbb{S}^n , we also state that how we construct RNGI on almost the whole $\mathbf{SO}(3)$. The orthogonality of $\mathbf{SO}(3)$ elements has a constraint on their trace that $\text{tr}(R) \in [-1, 3]$, so choose the main value of \arccos then we get a mapped $\gamma \in [0, \pi]$. But for those matrices with $\text{tr} = -1$, which represents a rotation with angle $= \pi$, the bijection between rotation vectors and orthogonal matrices does not hold anymore, leading to **nan** value of $\frac{\gamma}{2 \sin \gamma}$. Now we denote the set $\{R \in \mathbf{SO}(3) | \text{tr}(R) = -1\}$ and $\{\omega \in \mathfrak{so}(3) | |\omega| < \pi\}$ as $R(-1)$ and $\omega(\pi)$, the bijective Exp and Log can be constructed between

$$\begin{aligned} \text{Exp} : \omega(\pi) &\rightarrow [\mathbf{SO}(3) - R(-1)] \subset \mathbf{SO}(3), \\ \text{Log} : [\mathbf{SO}(3) - R(-1)] &\rightarrow \omega(\pi) \subset \mathfrak{so}(3). \end{aligned}$$

Every point $p \in \mathbf{SO}(3)$ gives a group-translation by group multiplication $p \cdot \mathbf{SO}(3)$, while the tangent space $T_p \mathbf{SO}(3)$ at p is concurrently given by the p -translation of Lie algebra. i.e.

$$p \cdot T_e \mathbf{SO}(3) = T_p \mathbf{SO}(3).$$

And for any tangent vector $v \in T_p \mathbf{SO}(3)$ and any other point $q \in \mathbf{SO}(3)$, their relative position of p is given by $p^{-1} \cdot (p, v, q) = (e, p^{-1}v, p^{-1}q)$. Then the Exp and Log map at p are translated from those at e :

$$\begin{aligned} \text{Exp}_p(v) &= p \cdot \text{Exp}_e(p^{-1}v), \\ \text{Log}_p(q) &= p \cdot \text{Log}_e(p^{-1}q), \end{aligned}$$

For the random variable x_0 and x_1 , the geodesic interpolant $I(t; x_0, x_1)$ on $\mathbf{SO}(3)$ is expressed as

$$\begin{aligned} I(t; x_0, x_1) &= \text{Exp}_{x_0}(t \cdot \text{Log}_{x_0} x_1) \\ &= x_0 \cdot \text{Exp}_e[t \cdot \text{Log}_e(x_0^{-1} x_1)]. \end{aligned}$$

We can easily verify that Exp – Log map is length-preservable. So as $\text{Log}_e(x_0^{-1} x_1) \in \mathfrak{so}(3)$, the time-derivative of geodesic interpolant $I(t; x_0, x_1)$ is

$$\partial_t I(t; x_0, x_1) = x_0 \cdot \text{Exp}_e[t \cdot \text{Log}_e(x_0^{-1} x_1)] \cdot \text{Log}_e(x_0^{-1} x_1).$$

The left-invariant translation is given by matrix multiplication $x_0 \cdot \text{Exp}_e[t \cdot \text{Log}_e(x_0^{-1} x_1)]$, which is length-preserving, so we have

$$|\partial_t I(t; x_0, x_1)| = |\text{Log}_e(x_0^{-1} x_1)|.$$

By the Rodrigues' rotation formula and main value constraint, $|\text{Log}_e(x_0^{-1} x_1)| \in [0, \pi]$, then the expectation $\mathbb{E}(|\partial_t I(t; x_0, x_1)|)$ is also bounded, thus the integrable condition on $\mathbf{SO}(3)$ is verified.

Proof of proposition 10 By the definition of KL-divergence, we can calculate the time-derivative of $\text{KL}(\rho(t) \parallel \hat{\rho}(t))$ as

$$\frac{d}{dt} \text{KL}(\rho(t) \parallel \hat{\rho}(t)) = \frac{d}{dt} \int_{\mathcal{M}} \log \frac{\rho(t, x)}{\hat{\rho}(t, x)} \rho(t, x) dM(x).$$

Commute the time-differential and integral symbol and apply the chain rule, and notice that

$$\int_{\mathcal{M}} \partial_t \rho(t, x) dM(x) = \partial_t \int_{\mathcal{M}} \rho(t, x) dM(x) = \partial_t 1 = 0,$$

we have

$$\begin{aligned} \frac{d}{dt} \text{KL}(\rho(t) \parallel \hat{\rho}(t)) &= \int_{\mathcal{M}} \log \frac{\rho(t, x)}{\hat{\rho}(t, x)} \partial_t \rho(t, x) dM(x) \\ &\quad - \int_{\mathcal{M}} \frac{\rho(t, x)}{\hat{\rho}(t, x)} \partial_t \hat{\rho}(t, x) dM(x). \end{aligned}$$

Substitute the two transport equations into above expression, and use the integration by parts formula, we have

$$\begin{aligned} &\frac{d}{dt} \text{KL}(\rho(t) \parallel \hat{\rho}(t)) \\ &= \int_{\mathcal{M}} \langle \nabla \log \rho(t, x) - \nabla \log \hat{\rho}(t, x), v(t, x) \rangle_g \rho(t, x) dM(x) \\ &\quad - \int_{\mathcal{M}} \langle \nabla \frac{\rho(t, x)}{\hat{\rho}(t, x)}, \hat{v}(t, x) \rangle_g \hat{\rho}(t, x) dM(x). \end{aligned}$$

Apply the chain rule of Riemannian gradient to the second term, we have

$$\begin{aligned} &\int_{\mathcal{M}} \langle \nabla \frac{\rho(t, x)}{\hat{\rho}(t, x)}, \hat{v}(t, x) \rangle_g \hat{\rho}(t, x) dM(x) \\ &= \int_{\mathcal{M}} \langle \nabla \log \rho(t, x) - \nabla \log \hat{\rho}(t, x), \hat{v}(t, x) \rangle_g \rho(t, x) dM(x). \end{aligned}$$

Merge above two equations and base on the bilinear property of Riemannian metric g , we finally get the exact expression of the time derivative

$$\begin{aligned} &\frac{d}{dt} \text{KL}(\rho(t) \parallel \hat{\rho}(t)) \\ &= \int_{\mathcal{M}} \langle s(t, x) - \hat{s}(t, x), v(t, x) - \hat{v}(t, x) \rangle_g \rho(t, x) dM(x). \end{aligned}$$

Integration from $t = 0$ to $t = 1$, by the fact that $\rho(0)$ and $\hat{\rho}(0)$ denote the same prior distribution so the initial KL-divergence $\text{KL}(\rho(x, 0) \parallel \hat{\rho}(x, 0)) = 0$, the proof is completed.

Furthermore, we can model the discrepancy of the interpolating process and generating process in the sense of Wasserstein metric.

Proof of proposition 11 For any $f \in C^\infty(\mathcal{M})$,

$$\begin{aligned} |f(X_t) - f(\hat{X}_t)| &\leq \int_0^t |v(f)(X_s, s) - \hat{v}(f)(\hat{X}_s, s)| ds \\ &\leq \int_0^t (|v(f)(X_s, s) - v(f)(\hat{X}_s, s)| + |v(f)(\hat{X}_s, s) - \hat{v}(f)(\hat{X}_s, s)|) ds \\ &\leq \int_0^t (L|f(X_s) - f(\hat{X}_s)| + \sup_{s \in [0, 1]} \sup_{x \in \mathcal{M}} |v(f)(x, s) - \hat{v}(f)(x, s)|) ds. \end{aligned}$$

Gronwall's lemma gives

$$|f(X_t) - f(\hat{X}_t)| \leq e^{Lt} \sup_{s \in [0, 1]} \sup_{x \in \mathcal{M}} |v(f)(x, s) - \hat{v}(f)(x, s)|.$$

Hence let d_g be the metric induced by g , we have

$$d_g(X_t, \hat{X}_t) \leq e^{Lt} \sup_{s \in [0, t]} \sup_{x \in \mathcal{M}} |v(x, s) - \hat{v}(x, s)|_g.$$

Then we have

$$W_p(\mu_t, \hat{\mu}_t) \leq [\mathbb{E} d_g(X_t, \hat{X}_t)^p]^{\frac{1}{p}} \leq e^{Lt} \sup_{s \in [0, t]} \sup_{x \in \mathcal{M}} |v(x, s) - \hat{v}(x, s)|_g.$$

C Experiment Details

Below we list the hyperparameters used to set RNGI model in various experiments in Table 7 and Table 8, the generative performance metrics from Table 9 to Table 15, and the generative visualization from Figure 2 to Figure 7. We promise that all the experiments are reproducible and will release the code after the acceptance of the paper.

C.1 Parameter setting

Below the tables are the hyperparameters used to set the RNGI model in various experiments. Learning rate, weight decay, step and gamma, namely optimizing hyperparameters, are pre-searched by Optuna (Akiba et al., 2019) and then uniformly decided. And the searching interval for the four optimizing hyperparameters are $[0.0001, 0.01]$, $[0.001, 0.01]$, $\{2000, 2500, \dots, 4500, 5000\}$ and $\{0.4, 0.45, \dots, 0.85, 0.9\}$ respectively.

Table 7: Hyperparameters for the training of RNGI model on geographical datasets on \mathbb{S}^2 . a/b means a for velocity training and b for score training respectively and a single a means a for both velocity and score training.

| Parameters | Volcano | Earthquake | Flood | Fire |
|----------------|----------------|----------------|----------------|-------------|
| Layers | 5 | 5 | 5 | 7 |
| Hidden units | 512 | 512 | 512 | 512 |
| Activation | relu | relu | relu | tanh |
| Training steps | 100000 | 100000 | 100000 | 150000 |
| Batch size | 512 | 512 | 512 | 512 |
| Optimizer | RiemannianAdam | RiemannianAdam | RiemannianAdam | AdamW |
| Learning rate | 0.003/0.0003 | 0.003/0.0003 | 0.003/0.0003 | 0.003/0.001 |
| Weight decay | - | - | - | 0.004/0.01 |
| Scheduler | StepLR | StepLR | StepLR | StepLR |
| Step | 2500/1500 | 3000/1500 | 2500 | 4000/2500 |
| Gamma | 0.7/0.4 | 0.8/0.4 | 0.7 | 0.8/0.7 |

Table 8: Hyperparameters for the density generation experiment on $\mathbf{SO}(3)$ and modals interpolation experiments on both \mathbb{S}^2 and $\mathbf{SO}(3)$.

| Parameters | Density generation | Modals interpolation |
|----------------|--------------------|----------------------|
| Layers | 6 | 6 |
| Hidden units | 512 | 1024 |
| Activation | relu | relu |
| Training steps | 50000 | 50000 |
| Batch size | 512 | 1024 |
| Optimizer | AdamW | AdamW |
| Learning rate | 0.0005 | 0.0005 |
| Weight decay | 0.01 | 0.01 |
| Scheduler | StepLR | StepLR |
| Step | 2500 | 2500 |
| Gamma | 0.7 | 0.7 |

C.2 Distance metric results in density interpolation

Below the tables are the generation results measured by K – L divergence in the experiment of interpolation between mixture distribution on \mathbb{S}^2 and $\mathbf{SO}(3)$. The number at row m column n denotes the 'K – L divergence between the generated $\hat{\mathbb{V}}^n$ samples from \mathbb{V}^m and the ground truth \mathbb{V}^n ' (as well as \mathbb{W}), where the two numbers in row 32 column 32 are forward/backward results respectively.

Table 9: Generation results from E-SDE scheme 17 in the experiment of interpolation between VMF mixture distribution on \mathbb{S}^2 .

| centers | 8 | 16 | 32 | 64 |
|---------|--------|--------|---------------|--------|
| 8 | 0 | - | 0.0174 | 0.0117 |
| 16 | - | 0 | - | 0.0140 |
| 32 | 0.0065 | - | 0.0071/0.0161 | - |
| 64 | 0.0335 | 0.0161 | - | 0 |

Table 10: Generation results from ODE scheme 10 in the experiment of interpolation between VMF mixture distribution on \mathbb{S}^2 .

| Centers | 8 | 16 | 32 | 64 |
|---------|--------|--------|---------------|--------|
| 8 | 0 | - | 0.0013 | 0.0088 |
| 16 | - | 0 | - | 0.0198 |
| 32 | 0.0130 | - | 0.0143/0.0254 | - |
| 64 | 0.0067 | 0.0302 | - | 0 |

Table 11: Generation results from GRW scheme 15 in the experiment of interpolation between VMF mixture distribution on \mathbb{S}^2 .

| Centers | 8 | 16 | 32 | 64 |
|---------|--------|--------|---------------|--------|
| 8 | 0 | - | 0.4586 | 0.2885 |
| 16 | - | 0 | - | 0.1976 |
| 32 | 0.3436 | - | 0.1155/0.0892 | - |
| 64 | 0.5521 | 0.1907 | - | 0 |

Table 12: Generation results from ODE scheme 10 of RNGI-D model in the experiment of interpolation between wrapped Gaussian mixture distribution on $\mathbf{SO}(3)$.

| Centers | 8 | 16 | 32 | 64 |
|---------|---------|---------|-----------------|---------|
| 8 | 0 | - | 0.00091 | 0.00083 |
| 16 | - | 0 | - | 0.00098 |
| 32 | 0.00005 | - | 0.00241/0.00024 | - |
| 64 | 0.00003 | 0.00017 | - | 0 |

Table 13: Generation results from GRW scheme 15 of RNGI-D model in the experiment of interpolation between wrapped Gaussian mixture distribution on $\mathbf{SO}(3)$.

| Centers | 8 | 16 | 32 | 64 |
|---------|---------|---------|-----------------|---------|
| 8 | 0 | - | 0.00463 | 0.00360 |
| 16 | - | 0 | - | 0.00116 |
| 32 | 0.00088 | - | 0.00278/0.00092 | - |
| 64 | 0.00059 | 0.00168 | - | 0 |

Table 14: Generation results from ODE scheme 10 of RNGI-E model in the experiment of interpolation between wrapped Gaussian mixture distribution on $\mathbf{SO}(3)$.

| Centers | 8 | 16 | 32 | 64 |
|---------|---------|---------|-----------------|---------|
| 8 | 0 | - | 0.00336 | 0.00036 |
| 16 | - | 0 | - | 0.00093 |
| 32 | 0.00021 | - | 0.00320/0.00071 | - |
| 64 | 0.00013 | 0.00043 | - | 0 |

Table 15: Generation results from E-SDE scheme 17 of RNGI-E model in the experiment of interpolation between wrapped Gaussian mixture distribution on $\mathbf{SO}(3)$.

| Centers | 8 | 16 | 32 | 64 |
|---------|---------|---------|-----------------|---------|
| 8 | 0 | - | 0.01802 | 0.00513 |
| 16 | - | 0 | - | 0.00408 |
| 32 | 0.00102 | - | 0.01073/0.00139 | - |
| 64 | 0.00088 | 0.00684 | - | 0 |

C.3 Visualization

Below the figures are the generative visualization of RNGI models in both density generation experiments and density interpolation experiments. The order of subfigures in Figure 5 is EM-ODE, ES-ODE, EM-ESDE and ES-ESDE, and that in Figure 6 is $\mathbb{W}^{32} \rightarrow \mathbb{W}^8$, $\mathbb{W}^{64} \rightarrow \mathbb{W}^8$, $\mathbb{W}^{64} \rightarrow \mathbb{W}^{16}$ and $\mathbb{W}_{\{\mu_i\}}^{32} \rightarrow \mathbb{W}_{\{\nu_i\}}^{32}$ respectively, while the order in Figure 7 is the same but the generative directions are reversed.



Figure 2: The generative performance of RNGI model on \mathbb{S}^2 in the distribution connection experiment $\mathbb{V}^{64} \rightarrow \mathbb{V}^{16}$. Both of the observation angle and the order of subfigure are the same as Figure 1.



Figure 3: The generative performance of RNGI model on \mathbb{S}^2 in the distribution connection experiment $\mathbb{V}_{\{\mu_i\}}^{32} \rightarrow \mathbb{V}_{\{\nu_i\}}^{32}$. Both of the observation angle and the order of subfigure are the same as Figure 1.



Figure 4: The backward generative performance by the E-SDE scheme of RNGI model on \mathbb{S}^2 in the four distribution connection experiments. From left to right are $\mathbb{V}^8 \rightarrow \mathbb{V}^{32}$, $\mathbb{V}^8 \rightarrow \mathbb{V}^{64}$, $\mathbb{V}^{16} \rightarrow \mathbb{V}^{64}$ and $\mathbb{V}_{\{\mu_i\}}^{32} \rightarrow \mathbb{V}_{\{\nu_i\}}^{32}$.

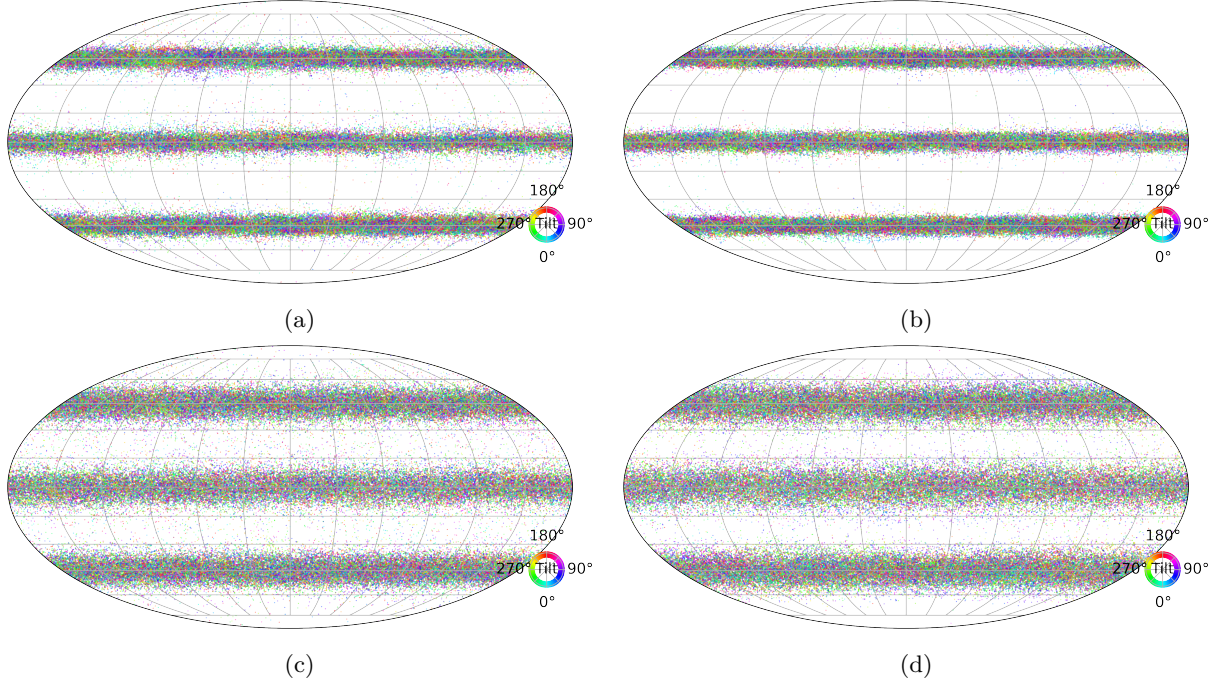


Figure 5: Generative performance of RNGI models on the line dataset of density generation experiment(1) on $\mathbf{SO}(3)$.

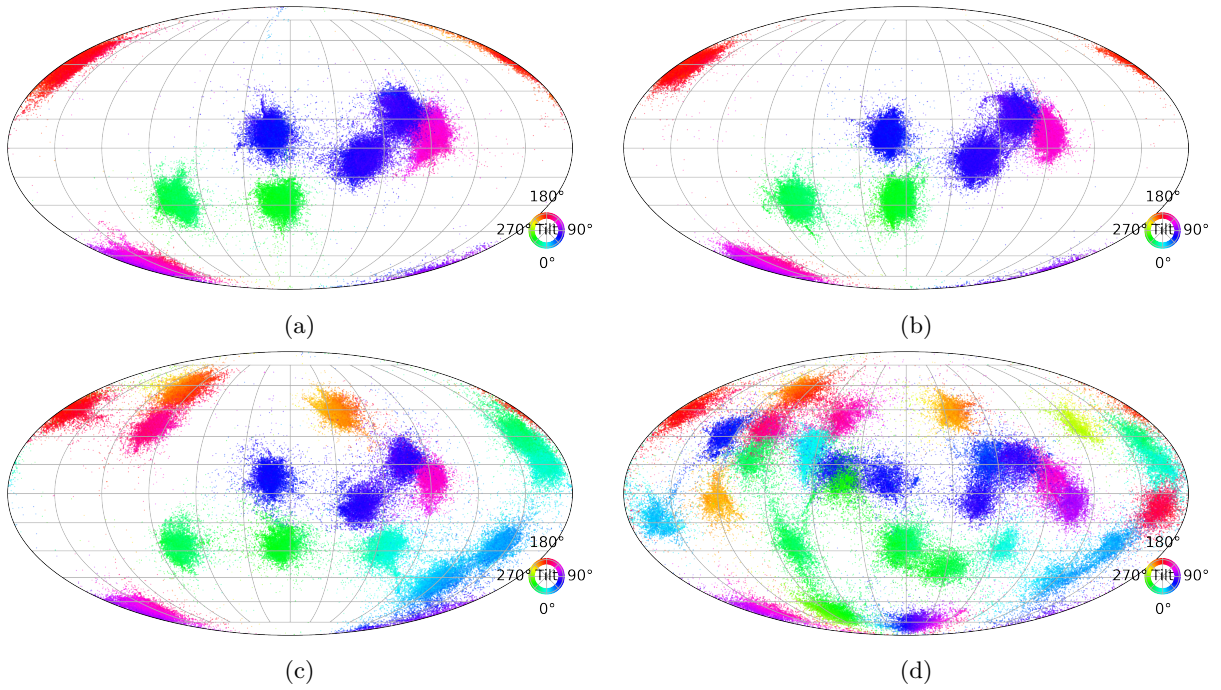


Figure 6: Generative performance of RNGI-E models by its ODE scheme equation 10 in the distribution connection experiment on $\mathbf{SO}(3)$.

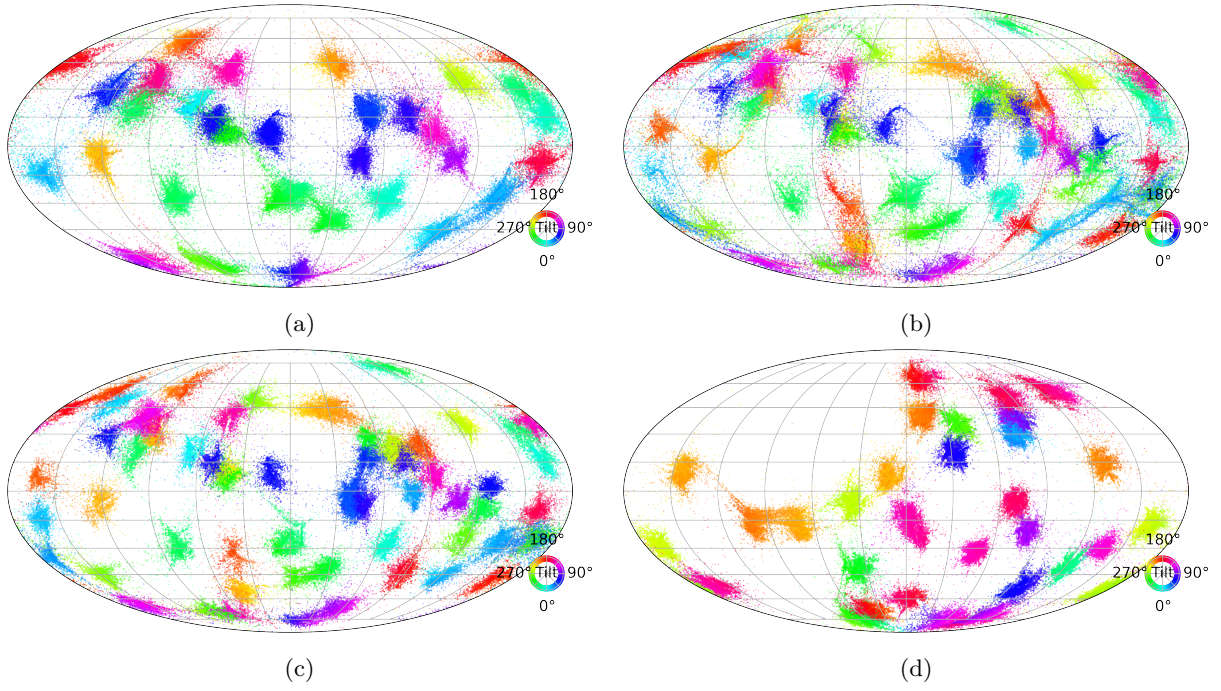


Figure 7: Generative performance of RNGI-D models by its ODE scheme equation 10 in the distribution connection experiment on $\mathbf{SO}(3)$.